Tensor networks and the numerical renormalization group

Andreas Weichselbaum
Physics Department, Arnold Sommerfeld Center for Theoretical Physics, and Center for NanoScience, Ludwig-Maximilians-Universität, 80333 Munich, Germany
(Received 14 September 2012; published 20 December 2012)

The full-density-matrix numerical renormalization group has evolved as a systematic and transparent setting for the calculation of thermodynamical quantities at arbitrary temperatures within the numerical renormalization group (NRG) framework. It directly evaluates the relevant Lehmann representations based on the complete basis sets introduced by Anders and Schiller [Phys. Rev. Lett. **95**, 196801 (2005)]. In addition, specific attention is given to the possible feedback from low-energy physics to high energies by the explicit and careful construction of the full thermal density matrix, naturally generated over a distribution of energy shells. Specific examples are given in terms of spectral functions (fdmNRG), time-dependent NRG (tdmNRG), Fermi-golden-rule calculations (fgrNRG) as well as the calculation of plain thermodynamic expectation values. Furthermore, based on the very fact that, by its iterative nature, the NRG eigenstates are naturally described in terms of matrix product states, the language of tensor networks has proven enormously convenient in the description of the underlying algorithmic procedures. This paper therefore also provides a detailed introduction and discussion of the prototypical NRG calculations in terms of their corresponding tensor networks.

DOI: 10.1103/PhysRevB.86.245124 PACS number(s): 05.10.Cc, 78.20.Bh, 75.20.Hr, 02.70.−c

I. INTRODUCTION

The numerical renormalization group (NRG)[1–3] is the method of choice for quantum impurity models. These consist of an interacting local system coupled to noninteracting typically fermionic baths, which in their combination can give rise to strongly correlated quantum-many-body effects. Through its renormalization group (RG) ansatz, its collective finite size spectra provide a concise snapshot of the physics of a given model from large to smaller energies on a logarithmic scale. A rich set of NRG analysis is based on these finite size spectra, including statistical quantities that can be efficiently computed within a single shell approach at an essentially discrete set of temperatures tied to a certain energy shell.[3–5] Dynamical quantities such as spectral functions, however, necessarily require to combine data from all energy scales. Since all NRG iterations contribute to a single final curve, traditionally it had not been clear how to achieve this in a systematic clean way, specifically so for finite temperatures.

The calculation of spectral properties within the NRG started with Oliveira and Wilkins[6,7] in the context of x-ray absorption spectra. This was extended to spectral functions at zero temperature by Sakai *et al.*[8] Finite temperature together with transport properties, finally, was introduced by Costi and Hewson.[4] An occasionally crucial feedback from small to large energy scales finally was taken care of by the explicit incorporation of the reduced density matrix for the remainder of the Wilson chain (DM-NRG) by Hofstetter.[9] While these methods necessarily combined data from all NRG iterations to cover the full spectral range, they did so through heuristic patching schemes. Moreover, in the case of finite temperature, these methods had been formulated in a single-shell setup that associates a well-chosen characteristic temperature that corresponds to the energy scale of this shell.

The possible importance of a true multishell framework for out-of-equilibrium situations had already been pointed out by Costi.[5] As it turns out, this can be implemented in a transparent systematic way using the complete basis sets, which where introduced by Anders and Schiller[10] for the feat of real-time evolution within the NRG (TD-NRG). This milestone development allowed for the first time to use the quasiexact method of NRG to perform real-time evolution to exponentially long time scales. It emerged together with other approaches to real-time evolution of quantum many-body systems such as the DMRG.[11,12] While more traditional single-shell formulations of the NRG still exist for the calculation of dynamical quantities using complete basis sets,[10,13] the latter, however, turned out significantly more versatile.[14–18] In particular, a clean multishell formulation can be obtained using the full-density-matrix (FDM) approach to spectral functions fdmNRG.[14] This essentially generalizes the DM-NRG[9] to a clean black-box algorithm, with the additional benefit that it allows to treat arbitrary finite temperatures on a completely generic footing. Importantly, the FDM approach can be easily adapted to related dynamical calculations, such as the time dependent NRG (tdmNRG) or Fermi-golden-rule calculations (fgrNRG). While specifically the fdmNRG and as well as the fgrNRG have already proven a very fruitful approach in the past,[14–16,19–22] so far, only the fdmNRG was presented in Ref. 14. The introduction and description of the remainder of the algorithms, which are fully embedded within the FDM approach, therefore represents a major purpose of this paper.

For the FDM approach, the underlying matrix product state (MPS) structure of the NRG[14,23] provides an extremely convenient framework. It allows for an efficient description of the necessary iterative *contractions* of larger tensor networks, i.e., summation over shared index spaces.[24] Moreover, since this quickly can lead to complex mathematical expressions if spelled out explicitly in detail, it has proven much more convenient to use a graphical representation for the resulting tensor networks.[24] In this paper, this is dubbed MPS diagrammatics. It concisely describes the relevant procedures that need to be performed, in practice, in the actual numerical simulation, and as such also represents a central part of this paper.

The paper then is organized as follows: the remainder of this section gives a brief introduction to the NRG, complete basis sets, its implication for the FDM approach, and the corresponding MPS description. This section also discusses the intrinsic relation of energy scale separation, efficiency of MPS, and area laws. Section II gives a brief introduction to MPS diagrammatics, and its implications for the NRG. Section III provides a detailed description of the FDM algorithms fdmNRG, tdmNRG, as well as fgrNRG in terms of their MPS diagrams. This also includes further related aspects, such as the generic calculation of thermal expectation values, or the generalization of fdmNRG to higher-order correlation functions. Section IV provides summary and outlook. A short appendix, finally, comments on the treatment of fermionic signs within tensor networks, considering that NRG typically deals with fermionic systems.

A. Numerical renormalization group and quantum impurity systems

The generic quantum impurity system (QIS) is described by the Hamiltonian

$$\hat{H}_{\mathrm{QIS}} = \underbrace{\hat{H}_{\mathrm{imp}} + \hat{H}_{\mathrm{cpl}}(\{\hat{f}_{0\mu}\})}_{\equiv \hat{H}_0} + \hat{H}_{\mathrm{bath}}, \tag{1}$$

which consists of a small quantum system (the *quantum impurity*) that is coupled to a non-interacting macroscopic reservoir $\hat{H}_{\mathrm{bath}} = \sum_{k\mu} \varepsilon_{k\mu} \hat{c}^\dagger_{k\mu} \hat{c}_{k\mu}$, e.g., a Fermi sea. Here, $\hat{c}^\dagger_{k\mu}$ creates a particle in the bath at energy $\varepsilon_{k\mu}$ with flavor μ, such as spin or channel, and energy index k. Typically, $\varepsilon_{k\mu} \equiv \varepsilon_k$. The state of the bath at the location $\vec{r} = 0$ of the impurity is given by $\hat{f}_{0\mu} \equiv \frac{1}{\mathcal{N}} \sum_k V_k \hat{c}_{k\mu}$ with proper normalization $\mathcal{N}^2 \equiv \sum_k V_k^2$. The coefficients V_k are determined by the hybridization coefficients of the impurity as specified in the Hamiltonian [e.g., see Eq. (4b) below]. The coupling $\hat{H}_{\mathrm{cpl}}(\{\hat{f}_{0\mu}\})$ then can act arbitrarily within the impurity system, while it interacts with the baths only through $\hat{f}^{(\dagger)}_{0\mu}$, i.e., its degrees of freedom at the location of the impurity. Overall, the Hilbert space of the typically interacting *local Hamiltonian* $\hat{H}_0$ in Eq. (1) is considered small enough so it can be easily treated exactly numerically.

The presence of interaction enforces the treatment of the full exponentially large Hilbert space. Within the NRG, this consists of a systematic state-space decimation procedure based on energy scale separation. (i) The continuum of states in the bath is coarse grained relative to the Fermi energy using the discretization parameter $\Lambda > 1$, such that with W the half-bandwidth of the Fermi sea, this defines a set of intervals $\pm W[\Lambda^{-(m-z+1)/2}, \Lambda^{-(m-z)/2}]$, each of which is eventually described by a single fermionic degree of freedom only. Here m is a positive integer, with the additional constant $z \in [0,1[$ introducing an arbitrary shift,[25,26] to be referred to as z shift. (ii) For each individual flavor μ then, the coarse grained bath can be mapped exactly onto a semi-infinite chain, with the first site described by $\hat{f}_{0\mu}$ and exponentially decaying hopping amplitudes t_n along the chain. This one-dimensional linear setup is called the Wilson chain,[1]

$$\hat{H}_N \equiv \hat{H}_0 + \sum_\mu \sum_{n=1}^{N} (t_{n-1} \hat{f}^\dagger_{n-1,\mu} \hat{f}_{n,\mu} + \mathrm{H.c.}), \tag{2}$$

where $\hat{H}_{\mathrm{QIS}} \simeq \lim_{N\to\infty} \hat{H}_N$. For larger n, it quickly holds[15,26]

$$\omega_n \equiv \lim_{n\gg 1} t_{n-1} = \frac{\Lambda^{z-1}(\Lambda - 1)}{\ln \Lambda} W \Lambda^{-\frac{n}{2}}, \tag{3}$$

where ω_n describes the smallest energy scale of a Wilson chain including all sites up to and including site n (described by $\hat{f}_{n\mu}$) for arbitrary Λ and z shift. In practice, all energies at iteration n are rescaled by the energy scale ω_n and shifted relative to the ground-state energy of that iteration. This is referred to as rescaled energies.

From the point of view of the impurity, the effects of the bath are fully captured by the hybridization function $\Gamma(\varepsilon) \equiv \pi \rho(\varepsilon) V^2(\varepsilon)$, which is assumed spin independent. For simplicity, a flat hybridization function is assumed throughout, i.e., $\Gamma(\varepsilon) = \Gamma \vartheta(W - |\varepsilon|)$, with the discretization following the prescription of Žitko and Pruschke.[26] If not indicated otherwise, all energies are specified in units of the (half-)bandwidth, which implies $W := 1$.

1. Single impurity Anderson model

The prototypical quantum impurity model applicable to the NRG is the single impurity Anderson model (SIAM).[27–30] It consists of a single interacting fermionic level (d level), i.e., the impurity,

$$\hat{H}_{\mathrm{imp}} = \sum_\sigma \varepsilon_{d\sigma} \hat{n}_{d\sigma} + U \hat{n}_{d\uparrow} \hat{n}_{d\downarrow} \tag{4a}$$

with level-position $\varepsilon_{d\sigma}$ and onsite interaction U. This impurity is coupled through the hybridization

$$\hat{H}_{\mathrm{cpl}} = \sum_\sigma \Big(\hat{d}^\dagger_\sigma \underbrace{\sum_k V_{k\sigma} \hat{c}_{k\sigma}}_{\equiv \sqrt{\frac{2\Gamma}{\pi}} \hat{f}_{0\sigma}} + \mathrm{H.c.} \Big) \tag{4b}$$

to a single spinful noninteracting Fermi sea, with Γ the total hybridization strength. Here, $\hat{d}^\dagger_\sigma$ ($\hat{c}^\dagger_{k\sigma}$) creates an electron with spin $\sigma \in \{\uparrow, \downarrow\}$ at the d level (in the bath with energy index k), respectively. Moreover, $\hat{n}_{d\sigma} \equiv \hat{d}^\dagger_\sigma \hat{d}_\sigma$, and $\hat{n}_{k\sigma} \equiv \hat{c}^\dagger_{k\sigma} \hat{c}_{k\sigma}$. At average occupation with a single electron, the model has three physical parameter regimes that can be accessed by tuning temperature: the free orbital regime (FO) at large energies allows all states at the impurity from empty to doubly occupied, the local moment regime (LM) at intermediate energies with a single electron at the impurity and the empty and double occupied state at high energy only accessible through virtual transitions, and the low-energy strong coupling (SC) fixed-point or Kondo regime, where the local moment is fully screened by the electrons in the bath into a quantum-many-body singlet.

B. Complete basis sets

Within the NRG, a complete many-body basis[10] can be constructed from the state space of the iteratively computed NRG eigenstates $\hat{H}_n |s\rangle_n = E^n_s |s\rangle_n$. With the NRG stopped at some final length N of the Wilson chain, the NRG eigenstates with respect to site $n < N$ can be complemented by the complete state space of the rest of the chain, $|e\rangle_n$, describing sites $n+1, \ldots, N$. The latter space will be referred to as the

environment, which due to energy scale separation will only weakly affect the states $|s\rangle_n$. The combined states,

$$|se\rangle_n \equiv |s\rangle_n \otimes |e\rangle_n, \tag{5}$$

then span the full Wilson chain. Within the validity of *energy scale separation*, one obtains[10]

$$\hat{H}_N|se\rangle_n \simeq E_s^n|se\rangle_n, \tag{6a}$$

i.e., the NRG eigenstates at iteration $n < N$ are, to a good approximation, also eigenstates of the full Wilson chain. This holds for a reasonably large discretization parameter $\Lambda \gtrsim 1.7$.[1,3,31]

With focus on the iteratively *discarded* state space, this allows to build a complete many-body eigenbasis of the full Hamiltonian,[10]

$$\mathbf{1}^{(d_0 d^N)} = \sum_{se,n} |se\rangle^{\mathrm{DD}}_{n\,n}\langle se|, \tag{6b}$$

where $d_0 d^N$ describes the full *many-body* Hilbert space dimension of the Hamiltonian H_N. Here d refers to the state space dimension of a single Wilson site, while d_0 refers to the state space dimension of the local Hamiltonian $\hat{H}_0$, which in addition to $\hat{f}_0$ also fully incorporates the impurity [cf. Eq. (1)]. It is further assumed that the local Hamiltonian H_0 is never truncated, i.e., truncation sets in for some $n = n_0 > 0$. Therefore, by construction, the iterations $n' < n_0$ do not contribute to Eq. (6b). At the last iteration $n = N$, all states are considered discarded by definition.[10] The truncation at intermediate iterations, finally, can be chosen either with respect to some threshold number N_{K} of states to keep, while nevertheless respecting degenerate subspace, or, preferentially, with respect to an energy threshold E_{K} in rescaled energies [cf. Eq. (3)]. The latter is a dynamical scheme which allows for a varying number of states depending on the underlying physics.

The completeness of the state space in Eq. (6b) can be easily motivated by realizing that at every NRG truncation step, by construction, the discarded space (eigenstates at iteration n with largest energies) is orthogonal to the kept space (eigenstates with lowest eigenenergies). The subsequent refinement of the kept space at later iterations will not change the fact, that the discarded states at iteration n remain orthogonal to the state space generated at later iterations. This systematic iterative truncation of Hilbert space while building up a complimentary complete orthogonal state space is a defining property of the NRG, and as such depicted schematically in Fig. 1.

C. Identities

This section deals with notation and identities related to the complete basis sets within the NRG. These are essential when directly dealing with Lehmann representations for the computation of thermodynamical quantities. While the combination of two basis sets discussed next simply follows Ref. 10, this section also introduces the required notation. The subsequent Sec. I D then derives the straightforward generalization to multiple sums over Wilson shells.

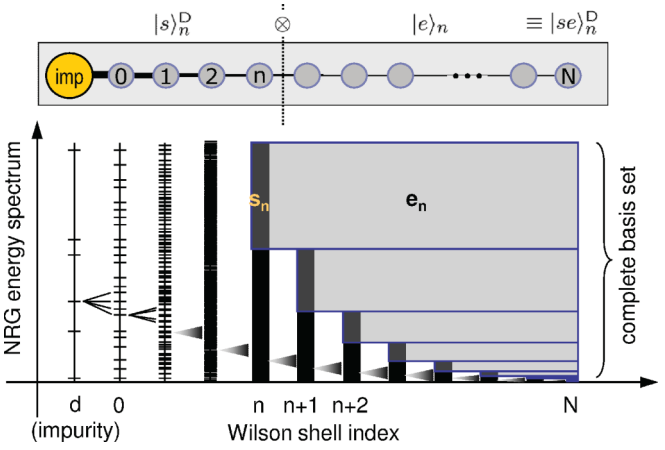

FIG. 1. (Color online) Iterative construction of complete basis set[10] within the NRG by collecting the *discarded* state spaces $|s\rangle_n^{\mathrm{D}}$ from all iterations $n \leqslant N$ (black space at the left of the gray blocks). For a given iteration n, these are complimented by the environment $|e\rangle_n$ for the rest of the system $n' > n$, i.e., starting from site $n+1$ up to the overall chain length N considered (gray blocks). In a hand-waving picture, by adding site $n+1$ to the system of sites $n' \leqslant n$, this site introduces a new lowest energy scale to the system, with the effect that existing levels become split within a narrow energy window (indicated by the spread of levels from one iteration to the next). The impurity, and also the first few sites can be considered exactly with a manageable total dimension of its Hilbert space still. Yet as the state space grows exponentially, truncation quickly sets in. The *discarded* state spaces then, when collected, form a complete basis. At the last iteration, where NRG is stopped, by definition, all states are considered discarded.

Given the complete basis in Eq. (6), it holds[10]

$$\underbrace{\sum_{se} |se\rangle^{\mathrm{KK}}_{nn}\langle se|}_{\equiv \hat{P}_n^{\mathrm{K}}} = \sum_{n'>n}^{N} \underbrace{\sum_{se} |se\rangle^{\mathrm{DD}}_{n'n'}\langle se|}_{\equiv \hat{P}_{n'}^{\mathrm{D}}}. \tag{7}$$

Here, the state space projectors $\hat{P}_n^{\mathrm{X}}$ are defined to project into the kept ($\mathrm{X} = \mathrm{K}$) or discarded ($\mathrm{X} = \mathrm{D}$) space of Wilson shell n. This then allows to rewrite Eq. (7) more compactly as

$$\hat{P}_n^{\mathrm{K}} = \sum_{n'>n}^{(N)} \hat{P}_{n'}^{\mathrm{D}}, \tag{8}$$

where the upper limit in the summation, $n' \leqslant N$, is implied if not explicitly indicated. With this, two independent sums over Wilson shells can be reduced into a single sum over shells,[10]

$$\begin{aligned}
&\sum_{n_1,n_2} \hat{P}_{n_1}^{\mathrm{D}} \hat{P}_{n_2}^{\mathrm{D}} \\
&\quad = \sum_{(n_1=n_2)\equiv n} \hat{P}_n^{\mathrm{D}} \hat{P}_n^{\mathrm{D}} + \sum_{n_1>(n_2\equiv n)} \hat{P}_{n_1}^{\mathrm{D}} \hat{P}_n^{\mathrm{D}} + \sum_{(n_1\equiv n)<n_2} \hat{P}_n^{\mathrm{D}} \hat{P}_{n_2}^{\mathrm{D}} \\
&\quad = \sum_n \left(\hat{P}_n^{\mathrm{D}} \hat{P}_n^{\mathrm{D}} + \hat{P}_n^{\mathrm{K}} \hat{P}_n^{\mathrm{D}} + \hat{P}_n^{\mathrm{D}} \hat{P}_n^{\mathrm{K}} \right) \\
&\quad \equiv \underbrace{\sum_n}_{\equiv \sum_n'} \sum_{\mathrm{XX}'}^{\neq \mathrm{KK}} \hat{P}_n^{\mathrm{X}} \hat{P}_n^{\mathrm{X}'}.
\end{aligned} \tag{9}$$

For simplified notation, the prime in the last single sum over Wilson shells ($\sum_n'$) indicates that also the kept-sectors are included in the sum over Wilson shells, yet excluding the all-kept sector $\mathrm{XX}' \neq \mathrm{KK}$, since this sector is refined still in later iterations.[10,14]

While Eq. (9) holds for the entire Wilson chain, exactly the same line of arguments can be repeated starting from some arbitrary but fixed reference shell n, leading to

$$\hat{P}_n^{\mathrm{K}}\hat{P}_n^{\mathrm{K}} = \sum_{n_1,n_2>n}^{N} \hat{P}_{n_1}^{\mathrm{D}}\hat{P}_{n_2}^{\mathrm{D}} = \sum_{\tilde{n}>n}^{N\,\prime} \hat{P}_{\tilde{n}}^{\mathrm{X}}\hat{P}_{\tilde{n}}^{\mathrm{X}'}, \tag{10}$$

where Eq. (8) was used in the first equality. Here the product of the two identical projectors $\hat{P}_n^{\mathrm{K}}$ on the LHS of Eq. (10) needs to be understood in the later context, where the two projectors are separated by other operators still [hence the LHS of Eq. (10) does not trivially reduce to a single projector]. The same also applies for the generalization in Eq. (12) below.

D. Generalization to multiple sums over shells

Consider the evaluation of some physical correlator that requires $m > 2$ insertions of the identity in Eq. (6b) in order to obtain a simple Lehmann representation. Examples in that respect are tdmNRG or (higher-order) correlation functions, as discussed later in the paper. In all cases, the resulting independent sum over arbitrarily many identities as in Eq. (6b) can always be rewritten as a *single* sum over Wilson shells. The latter is desirable since energy differences, such as they occur in the Lehmann representation for correlation functions, should be computed within the same shell, where both contributing eigenstates are described with comparable energy resolution.

Claim. Given m full sums as in Eq. (6b), this can be rewritten in terms of a single sum over a Wilson shell n, such that Eq. (9) generalizes to

$$\sum_{n_1,\ldots,n_m}^{N} \hat{P}_{n_1}^{\mathrm{D}_1}\ldots\hat{P}_{n_m}^{\mathrm{D}_m} = \underbrace{\sum_{\tilde{n}}^{N}\sum_{\mathrm{X}_1\cdots\mathrm{X}_m}^{\neq \mathrm{K}_1\ldots\mathrm{K}_m}}_{\equiv\sum_{\tilde{n}}'} \hat{P}_{\tilde{n}}^{\mathrm{X}_1}\ldots\hat{P}_{\tilde{n}}^{\mathrm{X}_m}, \tag{11}$$

where again the prime in the last single sum over Wilson shells ($\sum_n'$) indicates that *all* states are to be included within a given iteration n, while only excluding the all-kept sector $\mathrm{X}_1,\ldots,\mathrm{X}_m \neq \mathrm{K},\ldots,\mathrm{K}$. Note that via Eq. (8), the left-hand side of Eq. (11) can be rewritten as

$$\hat{P}_{n_0-1}^{\mathrm{K}_1}\ldots\hat{P}_{n_0-1}^{\mathrm{K}_m} = \sum_{n_1,\ldots,n_m} \hat{P}_{n_1}^{\mathrm{D}}\ldots\hat{P}_{n_m}^{\mathrm{D}},$$

where $n_0 > 0$ is the first iteration where truncation sets in. This way, $\hat{P}_{n_0-1}^{\mathrm{K}}$ refers to the full Hilbert space still. Proving Eq. (11) hence is again equivalent to proving for general n that

$$\hat{P}_n^{\mathrm{K}_1}\ldots\hat{P}_n^{\mathrm{K}_m} = \sum_{n_1,\ldots,n_m>n} \hat{P}_{n_1}^{\mathrm{D}}\ldots\hat{P}_{n_m}^{\mathrm{D}} = \sum_{\tilde{n}>n}' \hat{P}_{\tilde{n}}^{\mathrm{X}_1}\ldots\hat{P}_{\tilde{n}}^{\mathrm{X}_m}, \tag{12}$$

with the upper limit for each sum over shells, $n_i \leqslant N$ and $\tilde{n} \leqslant N$, implied, as usual. Therefore the sum in the center term, for example, denotes an independent sum $\sum_{n_i>n}^{N}$ for all n_i with $i = 1,\ldots,m$.

Proof. The case of two sums ($m = 2$) was already shown in Eq. (10). Hence one may proceed via induction. Assume, Eq. (12) holds for $m-1$. Then for the case m, one has in complete analogy to Eq. (9),

$$\begin{aligned}
&\hat{P}_n^{\mathrm{K}_1}\ldots\hat{P}_n^{\mathrm{K}_{m-1}}\cdot\hat{P}_n^{\mathrm{K}_m}\\
&= \Big(\sum_{n'>n}{}'\,\hat{P}_{n'}^{\mathrm{X}_1}\ldots\hat{P}_{n'}^{\mathrm{X}_{m-1}}\Big)\Big(\sum_{n_m>n}\hat{P}_{n_m}^{\mathrm{D}_m}\Big)\\
&= \sum_{\tilde{n}>n}{}'\,\hat{P}_{\tilde{n}}^{\mathrm{X}_1}\ldots\hat{P}_{\tilde{n}}^{\mathrm{X}_{m-1}}\big(\hat{P}_{\tilde{n}}^{\mathrm{D}_m}+\hat{P}_{\tilde{n}}^{\mathrm{K}_m}\big)+\hat{P}_{\tilde{n}}^{\mathrm{K}_1}\ldots\hat{P}_{\tilde{n}}^{\mathrm{K}_{m-1}}\hat{P}_{\tilde{n}}^{\mathrm{D}_m}\\
&\equiv \sum_{\tilde{n}>n}{}'\,\hat{P}_{\tilde{n}}^{\mathrm{X}_1}\ldots\hat{P}_{\tilde{n}}^{\mathrm{X}_m},
\end{aligned}$$

where from the second to the third line, it was used that

$$\sum_{n'>n}{}'\sum_{n_m>n} = \sum_{n<(\tilde{n}\equiv n'=n_m)}{}' + \sum_{n<(\tilde{n}\equiv n')<n_m}{}' + \sum_{n<(\tilde{n}\equiv n_m)<n'}{}',$$

and the last term in the third line followed from the inductive hypothesis. This proves Eq. (12).

Alternatively, the m independent sums over $\{n_1,\ldots n_m\}$ in Eq. (12) can be rearranged such, that for a specific iteration $\tilde{n}$, either one of the indices n_i may carry $\tilde{n}$ as minimal value, while all other sums range from $n_{i'} \geqslant \tilde{n}$. This way, by construction, the index n_i stays within the *discarded* state space, while all other sums $n_{i'}$ are unconstrained up to $n_{i'} \geqslant n_i = \tilde{n}$, thus represent either discarded at iteration $\tilde{n}$ or discarded at any later iteration that corresponds to the kept space at iteration $\tilde{n}$. From this, Eq. (12) also immediately follows.

E. Energy scale separation and area laws

By construction, the iterative procedure of the NRG generates an MPS representation for its energy eigenbasis.[23] This provides a direct link to the density matrix renormalization group (DMRG),[32,33] and consequently also to its related concepts of quantum information.[24] For example, it can be demonstrated that quite similar to the DMRG, the NRG truncation with respect to a fixed energy threshold E_{K} is also quasivariational with respect to the ground state of the semi-infinite Wilson chain.[15,31] Note furthermore that while DMRG typically targets a single global state, namely the ground state of the full system, at an intermediate step nevertheless it also must deal with large effective state spaces describing disconnected parts of the system. This again is very much similar to the NRG, which at every iteration needs to deal with many states.

Now, the success of variational MPS, i.e., DMRG, to ground-state calculations of quasi-one-dimensional systems is firmly rooted in the so-called area law for the entanglement or block entropy $S_A \equiv \mathrm{tr}(-\hat{\rho}_A \ln \hat{\rho}_A)$ with $\hat{\rho}_A = \mathrm{tr}_B(\hat{\rho})$.[34–36] In particular, the block entropy S_A represents the entanglement of some contiguous region A with the rest B of the entire system $A \cup B$ considered. This allows to explain, why MPS, indeed, is ideally suited to efficiently capture ground-state properties for quasi-one-dimensional systems.

In constrast to DMRG for real-space lattices, however, NRG references all energy scales through its iterative

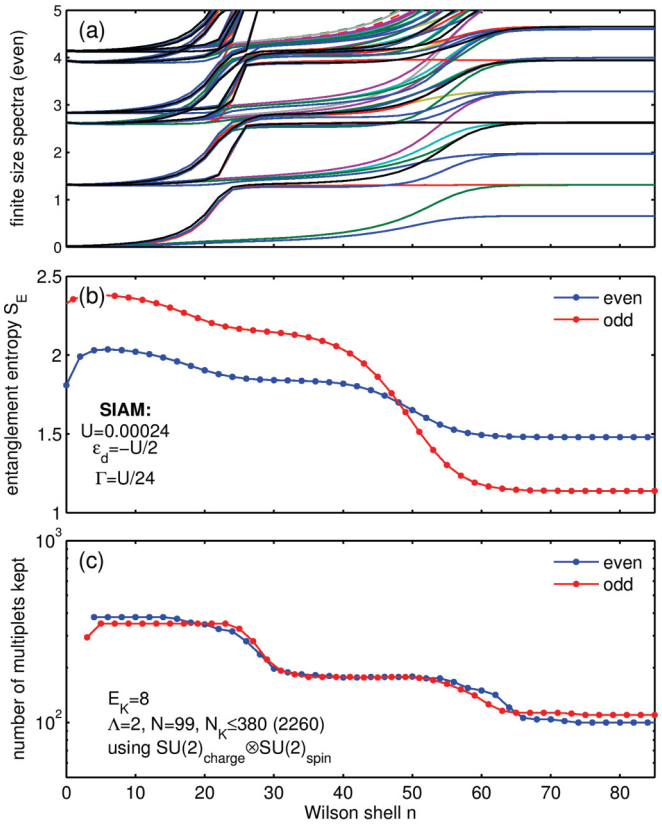

FIG. 2. (Color online) NRG and area law – analysis for the symmetric SIAM for the parameters as shown in panels (b) and (c) [cf. Eq. (4); all energies in units of bandwidth]. (a) The standard energy flow diagram of the NRG for even iterations where the different colors indicate different symmetry sectors. (b) The entanglement entropy S_n of the Wilson chain up to and including site $n < N$ with the rest of the chain, given the overall ground state ($N = 99$). Due to intrinsic even-odd alternations, even and odd iterations n are plotted separately. (c) The actual number of multiplets kept from one iteration to the next, using a dynamical truncation criteria with respect to a predefined fixed energy threshold E_K as specified. The calculation used $SU(2)_{spin} \otimes SU(2)_{charge}$ symmetry, hence the *actual* number of kept states is by about an order of magnitude larger [e.g., as indicated with the maximum number of multiplets kept, N_K in (c): the value in brackets gives the corresponding number of states].

diagonalization scheme. It zooms in towards the low-energy scales ("*ground-state properties*") of the full semi-infinite Wilson chain. Therefore given a Wilson chain of sufficient length N, without restricting the case, one may consider the fully mixed density matrix built from the ground-state space $|0\rangle_N$ of the last iteration, for simplicity. This then allows to analyze the entanglement entropy S_n of the states $|s\rangle_n$, i.e., the block of sites $n' < n$, with respect to its environment $|e\rangle_n$. The interesting consequence in terms of area law is that one expects the (close to) lowest entanglement entropy S_n for the stable low-energy fixed point, while one expects S_n to increase for higher energies, i.e., with *de*creasing Wilson shell index n.

This is nicely confirmed in a sample calculation for the SIAM, as demonstrated in Fig. 2. Figure 2(a) shows the standard NRG energy flow diagram (collected finite size spectra, here for even iterations), which clearly outlines the physical regimes of free orbital (FO, $n \lesssim 25$), local moment (LM, $25 \lesssim n \lesssim 60$), and strong coupling (SC, $n \gtrsim 60$) regime. Here, in order to have a sufficiently wide FO regime, a very small onsite interaction U was chosen relative to the bandwidth of the Fermi sea. Panel (b) shows the entanglement entropy S_n between system ($n' \leqslant n$) and environment ($n' > n$). Up to the very beginning or the very end of the actual chain (the latter is not shown), this shows a smooth monotonously decaying behavior versus energy scale. In particular, consistent with the area law for lowest-energy states, the entanglement is smallest once the stable low-energy fixed point is reached. Having chosen a dynamical (quasivariational)[15] truncation scheme with respect to a threshold energy E_K in rescaled energies [cf. Eq. (3)], the qualitative behavior of the entanglement entropy is also reflected in the number of states that one has to keep for some fixed overall accuracy, as shown in Fig. 2(c). Clearly, up to the very few first shells prior to truncation, the largest number of states must be kept at early iterations. While this is a hand-waving argument, this nevertheless confirms the empirical fact, that the first few Wilson shells with truncation are usually the most important, i.e., most expensive ones. Therefore, for good overall accuracy, all the way down to the low-energy sector, one must allow for a sufficiently large number of states to be kept at early iterations.

The entanglement entropy as introduced above together with the area law thus is consistent with the energy scale separation along the Wilson chain in [cf. Fig. 2(b)]. However, note that the specific value of the entanglement entropy is not a physical quantity, in that it depends on the discretization. While the entanglement entropy clearly converges to a specific value when including a sufficient number of states, it nevertheless sensitively depends on Λ. The smaller Λ, the larger the entanglement entropy S_n is going to be, since after all, the Wilson chain represents a gapless system. The overall qualitative behavior, however, is expected to remain the same, i.e., independent of Λ. Similar arguments hold for entanglement spectra and their corresponding entanglement flow diagram, which provide significantly more detailed information still about the reduced density matrices constructed by the bipartition into system and environment.[15]

F. Full density matrix

Given the complete NRG energy eigenbasis $|se\rangle_n^{\mathrm{D}}$, the full density matrix (FDM) at arbitrary temperature $T \equiv 1/\beta$ is simply given by[14]

$$\hat{\rho}^{\mathrm{FDM}}(T) = \sum_{sen} \frac{e^{-\beta E_s^n}}{Z} |se\rangle_{nn}^{\mathrm{DD}} \langle se|, \tag{13}$$

with $Z(T) \equiv \sum_{ne,s\in\mathrm{D}} e^{-\beta E_s^n}$. By construction of a thermal density matrix, all energies E_s^n from all shells n appear on an equal footing relative to a single global energy reference. Hence any prior iterative rescaling or shifting of the energies E_s^n, which is a common procedure within the NRG [cf. Eq. (3)], clearly must be undone. From a numerical point of view, typically the ground state energy at the last iteration $n = N$ for a given NRG run is taken as energy reference. In particular, this ensures numerical stability in that all Boltzmann weights are smaller or equal 1.

Note that the energies E_s^n are considered *independent* of the environmental index e. As a consequence, this leads to *exponentially large* degeneracies in energy for the states $|se\rangle_n$. The latter must be properly taken care of within FDM, as it contains information from all shells. By already tracing out the environment for each shell, this leads to[14]

$$\hat{\rho}^{\mathrm{FDM}}(T) = \sum_n \underbrace{\frac{d^{N-n} Z_n}{Z}}_{\equiv w_n} \sum_s \underbrace{\frac{e^{-\beta E_s^n}}{Z_n} |s\rangle^{\mathrm{DD}}_{nn} \langle s|}_{\equiv \rho_n^{\mathrm{D}}(T)}, \qquad (14)$$

with d the state-space dimension of a single Wilson site, and the proper normalization by the site-resolved partition function $Z_n(T) \equiv \sum_{s\in \mathrm{D}_n} e^{-\beta E_s^n}$ of the density matrices $\rho_n^{\mathrm{D}}(T)$ built from the discarded space of a specific shell n only. Therefore $\mathrm{tr}[\rho_n^{\mathrm{D}}(T)] = 1$, and also $Z(T) = \sum_n Z_n(T)$. Equation (14) then defines the weights w_n, which themselves represent a normalized distribution, i.e., $\sum_n w_n = 1$. Importantly, Eq. (14) demonstrates that the FDM is intrinsically specified through a range of energy shells n, whose weights w_n are fully determined.

1. Weight distribution w_n

The qualitative behavior of the weights w_n can be understood straightforwardly. With the typical energy scale of shell n given by

$$\omega_n = a\Lambda^{-n/2}, \qquad (15)$$

with a some constant of order 1. [cf. Eq. (3)], this allows to estimate the weights w_n as follows,

$$\ln(w_n) \simeq \ln(d^{N-n} e^{-\beta\omega_n}/Z) = (N-n)\ln(d) - \beta\omega_n + \mathrm{const.}$$

For a given temperature T, the shell n with maximum weight is determined by

$$\frac{d}{dn}\ln(w_n) \simeq -\ln(d) + \frac{a\beta\ln(\Lambda)}{2}\Lambda^{-n/2} \stackrel{!}{=} 0,$$

with the solution

$$a\Lambda^{-n^*/2} \simeq \frac{2\ln(d)}{\beta\ln(\Lambda)} \sim T, \qquad (16)$$

since the second term is $1/\beta$ times some constant of order 1. This shows that the weight distribution w_n is strongly peaked around the energy scale of given temperature T. With $T \equiv a\Lambda^{-n_T/2}$ and therefore $n_T \simeq n^*$, the distribution decays superexponentially fast towards larger energy scales $n \ll n_T$ (dominated by $e^{-\beta\omega_n}$ *with exponentially increasing* ω_n with decreasing n). Towards smaller energy scales $n \gg n_T$, on the other hand, the distribution w_n decays in a plain exponential fashion (dominated by d^{-n}, since with $\beta\omega_n \ll 1$, $e^{-\beta\omega_n} \to 1$). In contrast, for the single-shell approximation of the original formulation of DM-NRG[9] or derived approaches,[3,10,13] one uses the distribution $w_n \to \delta_{n,n_T}$.

An actual NRG simulation based on the SIAM is shown in Fig. 3. It clearly supports all of the above qualitative analysis. It follows for a typical discretization parameter Λ and local dimension d, that n_T is slightly smaller than n^*, i.e., towards larger energies to the left of the maximum in w_n, typically at the left onset of the distribution w_n, as is seen in the main panel in Fig. 3 (n_T is indicated by the vertical dashed line).

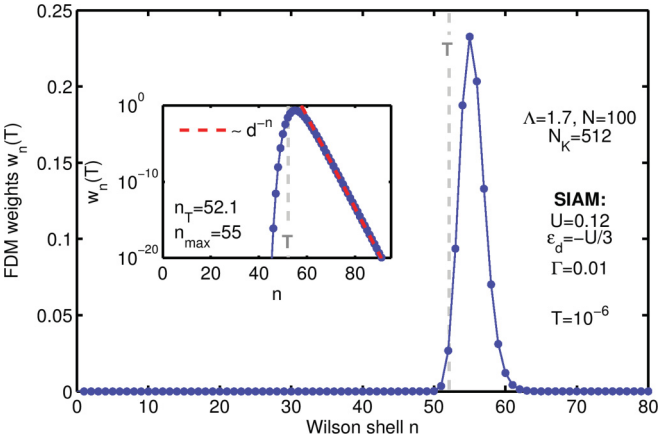

FIG. 3. (Color online) Typical FDM weight distribution calculated for the SIAM [cf. Eq. (4)] for the parameters as shown and temperature $T = 10^{-6}$ (all energies in units of bandwidth). The maximum number of states N_{K} kept at every iteration was taken constant. The distribution is strongly peaked around the energy shell $n^* \gtrsim n_T$, where n_T (indicated by vertical dashed line) corresponds to the energy scale of temperature as defined in the text. The inset plots the weights w_n on a logarithmic scale, which demonstrates the generic plain exponential decay for small energies $n > n_T$, and superexponentially fast decay towards large energies ($n < n_T$).

Within the shell n^* of maximum contribution to the FDM, therefore the actual temperature is somewhat larger relative to the energy scale of that iteration [note that this relates to the factor $\bar{\beta}$,[2,3] introduced by Krishna-murthy *et al.*[2] on heuristic grounds for the optimal *discrete* temperature representative for a single energy shell].

An important practical consequence of the exponential decay of the weights w_n for $n \gg n_T$ is that by taking a long enough Wilson chain to start with, fdmNRG *automatically* truncates the length of the Wilson chain at several iterations past n_T. Therefore the actual length of the Wilson chain N included in a calculation should be such that the full distribution w_n is sampled, which implies that w_n has dropped again at least down to $w_N \lesssim 10^{-3}$.

The weights w_n are fully determined within an NRG calculation, and clearly depend on the specific physical as well as numerical parameters. Most obviously, this includes the state space dimension d of a given Wilson site, and the discretization parameter Λ. However, the weights w_n also sensitively depend on the specific number of states kept from one iteration to the next. For example, the weights are clearly zero for iterations where no truncation takes place, which is typically the case for the very first NRG iterations that include the impurity. However, the weights also adjust automatically to the specific truncation scheme adopted, such as the quasivariational truncation based on an energy threshold E_{K}. In the case of fixed $N_{\mathrm{K}} = 512$ as in Fig. 3, note that if $d = 4$ times the number of states had been kept, i.e., $N_{\mathrm{K}} = 512 \to 2048$, this essentially would have shifted the entire weight distribution in Fig. 3 by one iteration to the right to lower energy scales, resulting in an improved spectral resolution for frequencies $\omega \lesssim T$.[14] For the latter purpose, however, it is sufficient to use an increased N_{K} at late iterations

only, where around the energy scale of temperature the weights w_n contribute mostly.

Furthermore, given a constant number N_K of kept states in Fig. 3, the weights w_n show a remarkably *smooth* behavior, irrespective of even or odd iteration n. This is somewhat surprising at first glance, considering that NRG typically does show pronounced even-odd behavior. For example, for the SIAM (see also Fig. 2), at even iterations an overall nondegenerate singlet can be formed to represent the ground state. Having no unpaired spin in the system, this typically lowers the energy more strongly as compared to odd iterations which do have an unpaired spin. Therefore, while even iterations show a stronger energy reduction in its low-energy states, its ground-state space consists of a single state. In contrast, for odd iterations the energy reduction by adding the new site is weaker, yet the ground state space is degenerate, assuming no magnetic field (Kramers degeneracy). In terms of the corresponding weight distribution for the full density matrix then, both effects balance each other, such that distribution of the FDM weights w_n results in a smooth function of the iteration n, as seen in Fig. 3.

In summary, above analysis shows that the density matrix generated by FDM is dominated by several shells around the energy scale of temperature. The physical information encoded in these shells can critically affect physical observables at much larger energies. This construction therefore *shall not* be shortcut in terms of the density matrix in the kept space at much earlier iterations, i.e., by using $\hat{H}|s\rangle_n^{\mathrm{K}} \simeq E_s^n|s\rangle_n^{\mathrm{K}}$ with the Boltzmann weights thus determined by the energies of the kept states. This can fail for exactly the reasons already discussed in detail with the DM-NRG construction by Hofstetter:[9] the low-energy physics can have important feedback to larger energy scales. To be specific, the physics at the low-energy scales on the order of temperature can play a decisive role on the decay channels of high-energy excitations. As a result, for example, the low-energy physics can lead to a significant redistribution of spectral weight in the local density of states at large energies.

2. *FDM representation*

The full thermal density matrix $\hat{\rho}_T^{\mathrm{FDM}}$ in Eq. (14) represents a regular operator with an intrinsic internal sum over Wilson shells. When evaluating thermodynamical expressions then, as seen through the discussions in Sec. I C and I D, its matrix elements must be calculated both with respect to discarded as well as kept states. While the former are trivial, the latter require some more attention. All of this, however, can be written compactly in terms of the projections in Eq. (7).

The reduced density matrix $\hat{\rho}_T^{\mathrm{FDM}}$ is a scalar operator, from which it follows,

$$\hat{P}_n^{\mathrm{X}}\hat{\rho}_T^{\mathrm{FDM}}\hat{P}_n^{\mathrm{X}'} \equiv \delta_{\mathrm{XX}'}\hat{R}_n^{\mathrm{X}}. \tag{17}$$

This defines the projections $\hat{R}_n^{\mathrm{X}}$ of $\hat{\rho}_T^{\mathrm{FDM}}$ onto the space $\mathrm{X} \in \{\mathrm{K},\mathrm{D}\}$ at iteration n, which are not necessarily normalized hence the altered notation. Like any scalar operator, thus also the projections $\hat{R}_n^{\mathrm{X}}$ carry a single label X only. The projection into the discarded space,

$$\hat{R}_n^{\mathrm{D}} \equiv \hat{P}_n^{\mathrm{D}}\hat{\rho}_T^{\mathrm{FDM}}\hat{P}_n^{\mathrm{D}} = w_n\hat{\rho}_n^{\mathrm{D}}(T), \tag{18}$$

by construction, is a fully diagonal operator as defined in Eq. (14). In kept space, however, the originally diagonal FDM acquires *nondiagonal* matrix elements in the NRG energy eigenbasis, thus leading to the block-diagonal scalar operator,

$$\hat{R}_n^{\mathrm{K}} \equiv P_n^{\mathrm{K}}\hat{\rho}_T^{\mathrm{FDM}}P_n^{\mathrm{K}} = \sum_{n'>n} w_{n'}\underbrace{\hat{P}_n^{\mathrm{K}}\hat{\rho}_{n'}^{\mathrm{D}}(T)\hat{P}_n^{\mathrm{K}}}_{\equiv\hat{\rho}_{n,n'}^{\mathrm{FDM}}(T)}, \tag{19}$$

with the properly normalized reduced density matrices,

$$\hat{\rho}_{n,n'}^{\mathrm{FDM}}(T) \equiv \operatorname*{tr}_{\{\sigma_{n+1},\ldots,\sigma_{n'}\}}\left[\hat{\rho}_{n'}^{\mathrm{D}}(T)\right]. \tag{20}$$

These are defined for $n' > n$ and, with respect to the basis of iteration n, are fully described within its kept space. Note that in the definition of the $\hat{\rho}_n^{\mathrm{D}}(T)$ in Eq. (14) the *environment* consisting of all sites $\tilde{n} > n'$ had already been traced out, hence in Eq. (20) only the sites $\tilde{n} = n+1,\ldots,n'$ remain to be considered. By definition, the reduced density matrices $\rho_{n,n'}^{\mathrm{FDM}}(T)$ are built from the effective basis $|s\rangle_{n'}^{\mathrm{D}}$ at iteration n', where subsequently the local state spaces $\sigma_{\tilde{n}}$ of sites $\tilde{n} = n',n'-1,\ldots,n+1$ are traced out in an iterative fashion.

The projected FDM operators $\hat{R}_n$, like other operators, are understood as operators in the basis $|s\rangle_n$, i.e., $\hat{R}_n^{\mathrm{X}} \equiv \sum_{s\in\mathrm{X}}(R_n^{\mathrm{X}})_{ss'}|s\rangle_{n\,n}\langle s'|$ (note the hat on the operator), while the bare matrix elements $(R_n^{\mathrm{X}})_{ss'} \equiv {}_n\langle s|\hat{R}_n^{\mathrm{X}}|s'\rangle_n$ are represented by R_n^{X} (by convention, written without hats). Overall then, the operator $\hat{R}_n$ can be written in terms of two contributions, (i) the contribution from iteration $n' = n$ itself (encoded in discarded space) and (ii) the contributions of all later iterations $n' > n$ (encoded in kept space at iteration n),

$$\hat{R}_n = \underbrace{w_n\hat{\rho}_n^{\mathrm{D}}(T)}_{=\hat{R}_n^{\mathrm{D}}} + \underbrace{\sum_{n'>n} w_{n'}\hat{\rho}_{n,n'}^{\mathrm{FDM}}(T)}_{=\hat{R}_n^{\mathrm{K}}} \tag{21a}$$

$$\equiv \sum_{n'\geqslant n} w_{n'}\hat{\rho}_{n,n'}^{\mathrm{FDM}}(T). \tag{21b}$$

In the last equation, for simplicity, the definition of $\hat{\rho}_{n,n'}$ for $n' > n$ in Eq. (20) has been extended to include the case $n' = n$, where $\hat{\rho}_{n,n} \equiv \hat{\rho}_n^{\mathrm{D}}(T)$.

II. MPS DIAGRAMMATICS

Given the complete basis sets which, to a good approximation, are also eigenstates of the full Hamiltonian, this allows to evaluate correlation functions in a text-book-like fashion based on their Lehmann representation. Despite the exponential growth of the many-body Hilbert space with system size, repeated sums over the entire Hilbert space nevertheless can be evaluated efficiently, in practice, due to the one-dimensional structure of the underlying MPS. [The situation is completely analogous to the product, say, of N matrices $A^{(n)}$, $n \in \{1,\ldots,N\}$, of dimension D, $(A^{(1)}A^{(2)}\ldots A^{(N)})_{ij} \equiv \sum_{k_1=1}^{D}\sum_{k_2=1}^{D}\cdots\sum_{k_N=1}^{D} A_{i,k_1}^{(1)}A_{k_1,k_2}^{(2)}\ldots A_{k_{N-1},j}^{(N)}$. There the sum over intermediate index spaces $k_1,\ldots,k_{N-1}$, in principle, also grows exponentially with the number of matrices. By performing the matrix product sequentially, however, this is no problem whatsoever.]

A. Basics and conventions

The NRG is based on an iterative scheme: given an (effective) many-body eigenbasis $|s\rangle_{n-1}$ up to and including site $n-1$ on the Wilson chain, a new site with a d-dimensional state space $|\sigma\rangle_n$ is added. Exact diagonalization of the combined system leads to the new eigenstates

$$|s_n\rangle = \sum_{s_{n-1},\sigma_n} A^{[\sigma_n]}_{s_{n-1},s_n} |\sigma\rangle_n |s\rangle_{n-1}. \tag{22}$$

Here, the coefficient space $A^{[\sigma_n]}_{s_{n-1},s_n}$ of the underlying unitary transformation is already written in standard MPS notation.[24,33] It will be referred to as A-tensor A_n which, by construction, is of rank 3. Equation (22) is depicted graphically in Fig. 4(a): two input spaces (s_{n-1} and σ_n to the left and at the bottom, respectively), and one output space s_n, as indicated by the arrows. Since by convention in this paper, NRG always proceeds from left to right, A-tensors always have the same directed structure. Therefore, for simplicity, all arrows will be skipped later in the paper. Furthermore, the block A_n, which depicts the coefficients of the A-tensor at given iteration, will be shrunk to a ternary node, resulting in the simplified elementary building block for MPS diagrams as depicted in panel Fig. 4(b). Finally, note that the start of the Wilson chain does not represent any specific specialization. The effective state space from the previous iteration is simply the vacuum state, as denoted by the (terminating) thick dot at the left of Fig. 4(c). The vacuum state represents a perfectly well-defined and normalized state, such that all subsequent contractions in the remainder of the panels in Fig. 4 apply identically without any specific further modification.

Figure 4(d) depicts the elementary contraction that represents the orthonormality condition,

$$\delta_{s_n,s'_n} = {}_n\langle s|s'\rangle_n = \sum_{s_{n-1},\sigma_n} A^{[\sigma_n]}_{s_{n-1},s'_n} A^{[\sigma_n]*}_{s_{n-1},s_n}, \tag{23}$$

again, with Fig. 4(e) a cleaned-up version, but otherwise exactly the same as Fig. 4(d). By graphical convention, contractions, i.e., summation over shared index or state spaces, are depicted by lines connecting two tensors. Note that in order to preserve the directedness of lines in Fig. 4(d), it is important with respect to bra-states, that all arrows on the A^*-tensor belonging to bra-states are fully reversed. For the remainder of the paper, however, this is of no further importance.

The contraction in Figs. 4(d) and 4(e) therefore results in an identity matrix, given that all input spaces of the A-tensor are contracted. For a mixed contraction, such as one input and one output state space, on the other hand, as indicated in Fig. 4(f), this results in a reduced density matrix. There the sum over the state space s_n is typically weighted by some normalized, e.g., thermal, weight distribution ρ_s, as indicated by the short dash across the line representing s_n together with the corresponding weights ρ_s.

Figures 4(g)–4(i) describe matrix representations of an operator B in the combined effective basis s_n for a local operator acting within σ_n [see Figs. 4(g) and 4(h)], or for an operator that acted at some earlier site, such that it already exists in the matrix representation of the basis s_{n-1}. For the latter case, the contraction in Fig. 4(h) typically occurred at some earlier iteration, with subsequent *iterative*

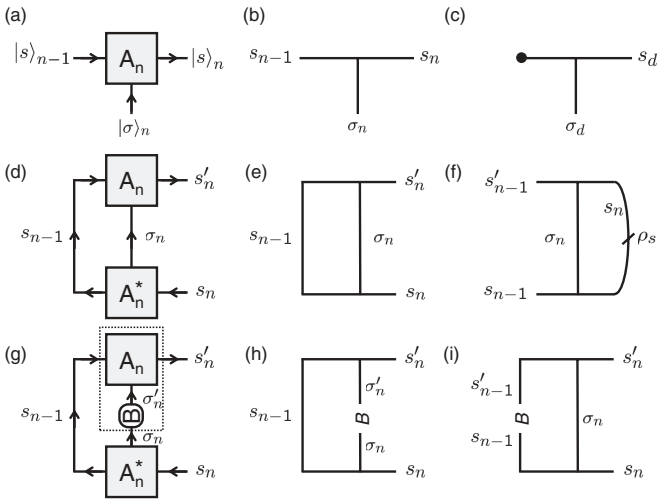

FIG. 4. Basic MPS diagrammatics. (a) Iteration step in terms of A-tensor. The coefficient space (A-tensor) for given iteration n is denoted by A_n, and incoming and outgoing state spaces are indicated by arrows. (b) Cleaned up simplified version of diagram in panel (a). Panel (c) indicates the first A-tensor in an MPS, in case it has the vacuum state to its left, which is denoted by a (terminating) thick dot. Here, trivially $|\sigma\rangle_d \equiv |s\rangle_d$ [with $|s\rangle_0$ for $n=0$ generated in the very next iteration with a Wilson chain in mind]. Panel (d) demonstrates the orthonormality condition of an A-tensor, $\sum_{\sigma_n}(A^{[\sigma_n]})^\dagger A^{[\sigma_n]} = \mathbf{1}$ [cf. Eq. (23)]. Panel (e) again is fully equivalent to (d). Panel (f) depicts a reduced density matrix. Panel (g) represents the evaluation of matrix elements of a local operator $\hat{B}$ at site n in the effective state space s_n. Panel (h) again is a cleaned up simplified version of (g). Panel (i) is similar to (g) and (h), except that the operator $\hat{B}$ was assumed to act at earlier sites on the Wilson chain, such that here B already describes the matrix elements in the effective basis s_{n-1}, and hence contracts from the left.

propagation of the matrix elements as in Fig. 4(i) for each later iteration. Contractions of a set of tensors are always performed sequentially, combining two tensors at a time.[24] In the case of Figs. 4(g)–4(i), the operator B, represented in the state space of σ'_n [s'_{n-1}] in Figs. 4(g) and 4(h) [Fig. 4(i)],

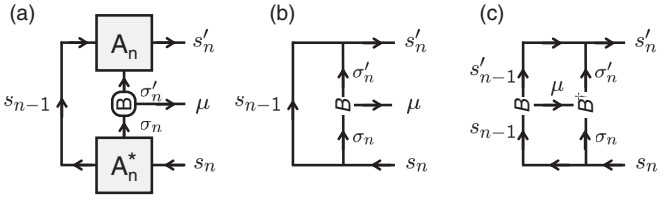

FIG. 5. Basic MPS diagrammatics in the presence of non-Abelian symmetries. (a) Representation of an irreducible operator $\hat{B}$ that acts within the local basis σ_n in the effective basis s_n. Being an irreducible operator, a third open index emerges, both for the representation of the local operator B (right incoming index to $B_{\sigma_n,\sigma'_n,\mu} \equiv \langle\sigma_n|\hat{B}^\mu|\sigma'_n\rangle$) as well as for the overall contracted effective representation with the open indizes $B_{s_n,s'_n,\mu}$, where μ identifies the spinor component in the irreducible operator $\hat{B}$. (b) Simplified version of (a), but exactly the same otherwise. (c) Contraction into a scalar representation of an operator B in the effective representation s_{n-1}, which acts at some site $n' < n$ with operator $B^\dagger$, which acts at site n. With $\hat{B}\cdot\hat{B}^\dagger \equiv \sum_\mu \hat{B}_\mu \cdot \hat{B}^\dagger_\mu$ a scalar operator, the result is a scalar operator of rank two in the indices (s_n, s'_n).

respectively, is contracted first, as indicated by the dashed box in Fig. 4(g). This is followed by the simultaneous contraction of the pair of indices (s_{n-1},σ_n). This way, the cost of the contraction in panels (g)–(i) scales like $\mathcal{O}(D^3)$,[24] where D represents the matrix dimension for the state spaces s_{n-1} and s_n (here considered to be the same, for simplicity).

For the NRG it is crucially important to use Abelian and non-Abelian symmetries for numerical efficiency.[1,17–19,37,38] Figure 5 therefore presents elementary tensor contractions in the presence of non-Abelian symmetries.[37] There the basis transformations in terms of the A-tensors A_n respect the underlying fusion rules for non-Abelian symmetries. Moreover, elementary operators $\hat{B}$ typically become irreducible operator sets $\{\hat{B}_\mu\}$ which are described in terms of a spinor with operator components labeled by the index μ [see Fig. 5(a)]. Using Wigner-Eckart theorem, the arrows, for example, with the operator $\hat{B}$ in Fig. 5(a) imply the underlying Clebsch-Gordan coefficient $(\sigma_n|\mu,\sigma_n')$.[37] In case of a scalar operator $\hat{B}$, the spinor reduces to a single operator, hence μ reduces to a singleton dimension which can be stripped. In that case, the third index to the center right of Figs. 5(a) and 5(b) can be removed, resulting in the equivalent diagrams in Figs. 4(g) and 4(h). Figure 5(c), finally, shows the contraction of two irreducible operator sets into a scalar operator $\hat{B}\cdot\hat{B}^\dagger \equiv \sum_\mu \hat{B}_\mu\cdot\hat{B}_\mu^\dagger$, again represented in the combined effective basis s_n. Here the operator $\hat{B}$ is considered to have acted once at some earlier site, whereas its daggered version acts on the current local site n. Note that again the daggered (conjugated) version has all its arrows reversed where, in addition, in the MPS diagram the dagger indicates, that the operator $B^\dagger$ as compared to B has already been also flipped upside down.

The only essential difference when using non-Abelian symmetries with MPS diagrammatics is the emergence of extra indices (lines) with respect to irreducible operators (index μ above). The underlying A-tensors, of course, need to respect the fusion rules of the symmetries employed, but on the level of an MPS diagram, this is implied. A detailed introduction to non-Abelian symmetries and its application to the NRG has been presented in Ref. 37. Therefore for the rest of this paper, for simplicity, no further reference to non-Abelian symmetries will be made, with all tensor networks based on the elementary contractions already presented in Fig. 4.

III. FDM APPLICATIONS

A. Spectral functions

Consider the retarded Green's function

$$G^R_{BC}(t) \equiv -i\vartheta(t)\underbrace{\langle \hat{B}(t)\hat{C}^\dagger\rangle_T}_{\equiv G_{BC}(t)}, \tag{24}$$

which may be considered the first term in the fermionic Green's function $G^R(t) = -i\vartheta(t)\langle\{\hat{B}(t),\hat{C}^\dagger\}\rangle_T$. Here, $\vartheta(t)$ is the Heaviside step function, and $\hat{B}(t)\equiv e^{i\hat{H}t}\hat{B}e^{-i\hat{H}t}$, where, as usual, the Hamiltonian $\hat{H}$ of the system is considered time-independent. In Eq. (24), an operator $\hat{C}^\dagger$ acts at time $t=0$ on a system in thermal equilibrium at temperature T, described by the thermal density matrix $\hat{\rho}(T) = e^{-\beta\hat{H}}/Z(T)$ with $\langle * \rangle_T \equiv \mathrm{tr}[\hat{\rho}(T) *]$. The system then evolves to some time $t>0$, where a possibly different operator $\hat{B}$ is applied. The overlap with the original time evolved wave function then defines the retarded correlation function of the two events. Fourier transformed into frequency space, $G^R_{BC}(\omega)\equiv\int dt\, e^{i\omega t}G^R_{BC}(t)$, its spectral function is given by

$$\begin{aligned} A_{BC}(\omega) &= \int \frac{dt}{2\pi} e^{i\omega t} G_{BC}(t) \\ &= \int \frac{dt}{2\pi} e^{i\omega t}\,\mathrm{tr}[\hat{\rho}(T) e^{i\hat{H}t}\hat{B}e^{-i\hat{H}t}\hat{C}^\dagger], \end{aligned} \tag{25}$$

which for real operators $\hat{B}$ and $\hat{C}$ is equivalent to $A_{BC}(\omega) = -\frac{1}{\pi}\mathrm{Im}G^R_{BC}(\omega)$. When evaluated in the full many-body eigenbasis, in principle, this requires the insertion of two identities, (i) to evaluate the trace and (ii) in between the operators $\hat{B}$ and $\hat{C}^\dagger$ to deal with the exponentiated Hamiltonian. For simplified, with the eigenbasis sets $\mathbf{1} = \sum_a |a\rangle\langle a| = \sum_b |b\rangle\langle b|$, the spectral function becomes

$$\begin{aligned} A_{BC}(\omega) &= \sum_{ab}\int \frac{dt}{2\pi} e^{i(\omega-E_{ab})t}\rho_a \langle a|\hat{B}|b\rangle\langle b|\hat{C}^\dagger|a\rangle \\ &\equiv \sum_{ab}\rho_a B_{ab}C^*_{ab}\cdot\delta(\omega-E_{ab}), \end{aligned} \tag{26}$$

with $E_{ab}\equiv E_b - E_a$ and $\rho_a \equiv \frac{1}{Z}e^{-\beta E_a}$. By convention, as usual, operators carry hats, while matrix representations in a given basis have no hats ($\hat{B}$ versus B_{ab}). Equation (26) is referred to as the Lehmann representation of the correlation function in Eq. (24). In the case of equal operators, $\hat{B}=\hat{C}$, the spectral function is a strictly positive function, i.e., a spectral density. In either case, the integrated spectral function results in the plain thermodynamic expectation values,[14]

$$\int d\omega A_{BC}(\omega) = \sum_{ab}\rho_a\, B_{ab}C^*_{ab} = \langle\hat{B}\hat{C}^\dagger\rangle_T. \tag{27}$$

Now, using the complete NRG eigenbasis, $|a\rangle \to |se\rangle_n$ and $|b\rangle\to|s'e'\rangle_{n'}$, one may have been tempted of directly reducing the double sum in Eq. (26) to a single sum over Wilson shells using Eq. (9). This implies that the thermal weight would be constructed as $\rho_a(T)\sim e^{-\beta E_a}\to e^{-\beta E_s^{n,\mathrm{X}}}$ from both, the discarded (X = K) as well as the kept (X = K) space at iteration n. This, however, ignores a possible feedback from small to large energy scales which has been shown to be crucial in the NRG context.[9]

The solution is to take the FDM as it stands in Eq. (13). This, however, introduces yet another independent sum c over Wilson shells, in addition to a and b in Eq. (26) above,

$$A_{BC}(\omega) = \sum_{abc}\rho_{ca}B_{ab}C^*_{ac}\cdot\delta(\omega-E_{ab}). \tag{28}$$

The triple-sum over $\{a,b,c\}$ can be treated as in Eq. (11). With $\{a,b,c\}\to\{s,s',s_\rho\}_n \in \{\mathrm{XX'X}_\rho \neq \mathrm{KKK}\}$, nevertheless, $\mathrm{X}=\mathrm{X}_\rho$ are locked to each other since ρ itself represents a scalar operator, and by construction does not mix kept with discarded states. Therefore only the contributions $\mathrm{XX'}\neq\mathrm{KK}$ as known from a double sum remain. With

$$\begin{aligned} &\mathrm{tr}\left[\hat{\rho}_T^{\mathrm{FDM}}\hat{B}(t)\cdot\hat{C}^\dagger\right] \\ &\quad= \sum_n\sum_{\mathrm{XX'X}_\rho}\mathrm{tr}\Big[\underbrace{\hat{P}_n^{\mathrm{X}_\rho}\cdot\hat{\rho}_T^{\mathrm{FDM}}\cdot\hat{P}_n^{\mathrm{X}}}_{=\delta_{\mathrm{XX}_\rho}\hat{P}_n^{\mathrm{X}}}\hat{B}(t)\hat{P}_n^{\mathrm{X'}}\cdot\hat{C}^\dagger\Big], \end{aligned}$$

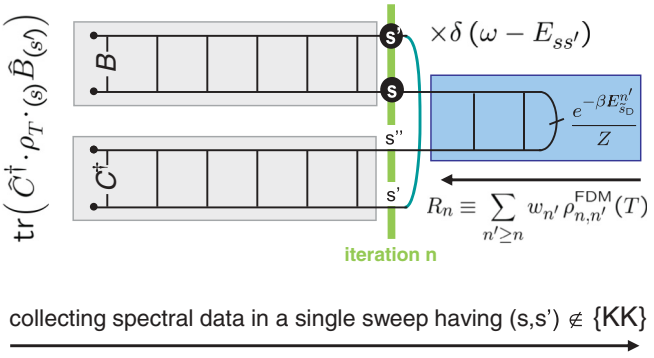

FIG. 6. (Color online) MPS diagram for calculating spectral functions using fdmNRG based on the Lehmann representation in Eq. (29). In general, spectral functions are preceded by an NRG *forward sweep*, which generates the NRG eigenbasis decomposition (horizontal lines; cf. Fig. 4). Correlation functions then require the evaluation of the matrix elements $\mathrm{tr}[\hat{C}\rho_T \cdot {}_{(s)}\hat{B}_{(s')}]$, as indicated at the left of the figure. The energies of the indices (states) s and s' are "probed" such that their difference determines the energy $\omega = E^n_{ss'} \equiv E^n_{s'} - E^n_s$ of an individual contribution to the spectral function, as indicated by the $\times\delta(\omega - E_{ss'})$ next to the indices s and s' in the upper right of the figure. The sum $\sum_{n'>n}$ in the discarded state space of $\hat{\rho}^{\mathrm{FDM}}(T)$, indicated to the lower right, results in the object R_n [cf. Eq. (21b)]. The individual contributions $\rho^{\mathrm{FDM}}_{n,n'}(T)$ are generated by the Boltzmann weights in the discarded space at iteration n', as indicated to the right. The contribution at $n' = n$, i.e., R^{D}_n, can simply be determined when needed. On the other hand, the cumulative contributions $n' > n$ are obtained in a simple prior *backward sweep*, starting from the last Wilson shell N included, as indicated by the small arrow pointing to the left. Having $n' > n$, this calculation always maps to the kept space, thus resulting in R^{K}_n. Finally, the spectral data is collected in a single forward sweep, as indicated at the bottom of the figure.

it follows for spectral functions (fdmNRG),[14]

$$A_{BC}(\omega) = \sum_{n,ss'}{}' [C^\dagger_n R_n]_{s's}(B_n)_{ss'}\,\delta\left(\omega - E^n_{ss'}\right), \qquad (29)$$

where the prime with the sum again indicates that only the combinations of states $ss' \in \mathrm{XX}' \neq \mathrm{KK}$ are to be considered at iteration n. To be specific, given the scalar nature of the projections $\hat{R}_n$, the first term implies the matrix product $(C^\dagger_n R_n)^{\mathrm{X'X}} \equiv (C^\dagger_n)^{\mathrm{X'X}} R^{\mathrm{X}}_n$.

The MPS diagram of the underlying tensor structure is shown in Fig. 6. Every leg of the "ladders" in Fig. 6 corresponds to an NRG eigenstate (MPS) $|s\rangle_n$ for some intermediate iteration n. The blocks for the MPS coefficient spaces (A-tensors) are no longer drawn, for simplicity [cf. Fig. 4]. The outer sum over the states s' in Eq. (29) corresponds to the overall trace. Hence the upper- and lower-most legs in Fig. 6 at iteration n carry the same state label s', as they are connected by a line (contraction). Furthermore, the inserted identity in the index s initially also would have been identified with two legs [similar to what is seen in Fig. 7 later]. At iteration n, however, the state space s directly hits the FDM, leading to the overlap matrix ${}^{\mathrm{X}}_n\langle s|\tilde{s}\rangle^{\tilde{\mathrm{X}}}_n = \delta_{s\tilde{s}}\delta_{\mathrm{X}\tilde{\mathrm{X}}}$ [hence this eliminates the second block from the top in Fig. 7]. As a result, only the single index s from the second complete sum remains in Fig. 6. The same argument applies for the index s''.

The two legs in the center of Fig. 6, finally, stem from the insertion of the FDM which can extend to all iterations $n' \geqslant n$. Note that the case $n' < n$ does not appear, since there the discarded state space used for the construction of the FDM is orthogonal to the state space s at iteration n. The trace over the environment at iteration n leads to the reduced (partial) density matrices R_n. Here, the environmental states $|e\rangle_{n'}$ for the density matrices $\rho^{\mathrm{D}}_{n'}(T)$ for $n' \geqslant n$ had already all been traced out, as pointed out with Eq. (14). The FDM thus reduces at iteration n to the scalar operator $R^{(\mathrm{X})}_n$ as introduced in Eq. (21).

In summary, by insisting on using the FDM in Eq. (13) this only leads to the minor complication that R^{K}_n needs to be constructed and included in the calculation. The construction of R^{K}_n, on the other hand, can be done in a simple prior backward sweep, which allows to generate R^{K}_n iteratively and thus efficiently. All of the R^{K}_n need to be stored for the later calculation of the correlation function. Residing in kept space, however, the computational overhead is negligible. The actual spectral data, finally, is collected in a single forward sweep, as indicated in Fig. 6.

1. *Exactly conserved sum rules*

By construction, FDM allows to exactly obey sum-rules for spectral functions as a direct consequence of Eq. (27) and fundamental quantum-mechanical commutator relations. For example, after completing the Green's function in Eq. (24) to a proper many-body correlation function for fermions, $G_d(t) \equiv -i\vartheta(t)\langle\{\hat{d}(t),\hat{d}^\dagger\}\rangle_T$, with $\hat{d}^\dagger$ creating an electron in level d at the impurity and $\{\cdot,\cdot\}$ the anticommutator, the integrated spectral function results in[14]

$$\int d\omega A(\omega) = \langle\{\hat{d},\hat{d}^\dagger\}\rangle_T = 1, \qquad (30)$$

due to the fundamental fermionic anticommutator relation, $\{\hat{d},\hat{d}^\dagger\} = 1$. In practice, Eq. (30) is obeyed exactly within numerical double precision noise (10^{-16}), which underlines the fact that the full exponentially large quantum many-body state space can be dealt with in practice, indeed. Note, however, that Eq. (30) holds by construction, and therefore it is not measure for convergence of an NRG calculation. The latter must be checked independently.[15]

2. *Implications for complex Hamiltonians*

The Hamiltonians analyzed by NRG are usually time-reversal invariant, and therefore can be computed using non-complex numbers. In case the Hamiltonian is not time-reversal invariant, i.e., the calculation becomes intrinsically complex, the A-tensors on the lower leg of the ladders for the operators $\hat{B}$ and $\hat{C}^\dagger$ in Fig. 6 must be complex conjugated (see also Fig. 4). Consequently, this implies for the FDM projections R_n, that in Fig. 6 its constituting A-tensors in the *upper* leg need to be complex conjugated.

B. Thermal expectation values

Arbitrary thermodynamic expectation values can be calculated within the fdmNRG framework, in principle, through Eq. (27). Given the spectral data on the left-hand side of Eq. (27), for example, this can be integrated to obtain the thermodynamic expectation value on the right-hand side of

Eq. (27). In practice, this corresponds to a simple sum of the nonbroadened discrete spectral data as obtained from fdmNRG. Using the plain discrete data has the advantage that it does not depend on any further details of broadening procedures which typically would introduce somewhat larger error bars otherwise.

For dynamical properties within the NRG, however, usually only *local operators* are of interest. That is, for example, the operators $\hat{B}$ or $\hat{C}$ in Eq. (27) act within the *local* Hamiltonian $\hat{H}_0$ [Wilson shell $n = 0$; cf. Eq. (1)], or within the very first Wilson sites $n < n_0$, where n_0 stands for the first Wilson shell where truncation sets in. For this early part of the Wilson chain, the weights w_n are identically zero. Consequently, the reduced thermal density matrix is fully described for iteration $n < n_0$ for arbitrary temperatures T by $R_n^{\mathrm{K}}(T)$ in kept space. For a given temperature, the aforementioned simple backward sweep to calculate R_n^{K} then already provides all necessary information for the simple evaluation of the thermal expectation value of any local operator $\hat{C}$ [e.g., $\hat{C} := \hat{B}\hat{C}^\dagger$ in Eq. (27)],

$$\langle \hat{C} \rangle_T = \mathrm{tr}\left[R_n^{(\mathrm{K})}(T) C_n^{(\mathrm{KK})}\right], \quad (n < n_0) \tag{31}$$

with $C_n^{(\mathrm{KK})}$ the matrix elements of the operator $\hat{C}$ in the kept space of iteration n. With no truncation yet at iteration n, the kept space is the only space available, i.e., represents the full state space up to iteration n [hence the brackets around the K's]. For strictly local operators acting within the state space of H_0, one has $\langle \hat{C} \rangle_T = \mathrm{tr}[R_0(T) C_0]$. The clear advantage of Eq. (31) is that once $R_n^{(\mathrm{K})}(T)$ has been obtained for given temperature, *any* local expectation value can be computed in a simple manner *without* the need to explicitly calculate the matrix elements of the operator $\hat{C}$ throughout the entire Wilson chain.

In Eq. (31), it was assumed that the operator $\hat{C}$ acts on sites $n \leqslant n_0$ only. This can be relaxed significantly, however, assuming that temperature is typically much smaller than the bandwidth of the system. In that case, the weight distribution w_n already also has absolutely negligible contribution at earlier iterations $n' \ll n_T$ which clearly stretches beyond n_0 (see Fig. 3 and discussion). Hence Eq. (31) can be relaxed to all iterations n for which $\sum_{n'<n} w_{n'} \ll 1$.

In the case that the operator $\hat{C}$ is not a local operator at all, but nevertheless acts locally on some specific Wilson site n, then using Eqs. (14) and (21) it follows for the general case,

$$\langle \hat{C} \rangle_T = \mathrm{tr}\left[R_n^{\mathrm{K}}(T) C_n^{\mathrm{KK}}\right] + \mathrm{tr}\left[R_n^{\mathrm{D}}(T) C_n^{\mathrm{DD}}\right] + c \sum_{n'<n} w_{n'}, \tag{32}$$

which corresponds to the partitioning of Eq. (14) given by $\sum_{n'} = \sum_{n'>n} + \sum_{n'=n} + \sum_{n'<n}$, respectively. The last term in Eq. (32) derives from the discarded state spaces for Wilson shells $n' < n$ at (much) larger energy scales. Therefore the fully mixed thermal average applies, such that the resulting constant $c \equiv \frac{1}{d}\,\mathrm{tr}_{\sigma_n}(\hat{C})$ is the plain average of the operator $\hat{C}$ in the local basis $|\sigma_n\rangle$ that it acts upon. To be specific, this derives from the trace over the environmental states $|e\rangle_n$ in Eq. (14). Equation (31) finally follows from Eq. (32), in that for $n < n_0$, by construction, due to the absence of truncation the second and third term in Eq. (32) are identically zero.

C. Time-dependent NRG

Starting from the thermal equilibrium of some initial (I) Hamiltonian $\hat{H}^{\mathrm{I}}$, at time $t = 0$ a quench at the location of the quantum impurity occurs, with the effect that for $t > 0$ the time-evolution is governed by a different final (F) Hamiltonian $\hat{H}^{\mathrm{F}}$. While initially introduced within the single-shell framework for finite temperature,[10] the same analysis can also be straightforwardly generalized to the multishell approach of fdmNRG. Thus the description here will focus on the FDM approach.

Given a quantum quench, the typical time-dependent expectation value of interest is

$$C(t) \equiv \langle \hat{C}(t) \rangle_T \equiv \mathrm{tr}[\rho^{\mathrm{I}}(T) \cdot e^{iH^{\mathrm{F}}t} \hat{C} e^{-iH^{\mathrm{F}}t}], \tag{33}$$

with $\hat{C}$ some observable. While the physically relevant time domain concerns the dynamics after the quench, i.e., $t > 0$, one is nevertheless free to extend the definition of Eq. (33) also to negative times. The advantage of doing so is, that the Fourier transform into frequency space of the $C(t)$ in Eq. (33) defined for arbitrary times becomes purely real, as will be shown shortly. With this the actual time-dependent calculation can be performed *in frequency space first* in a simple and for the NRG natural way,

$$C(\omega) = \int \frac{dt}{2\pi} e^{i\omega t}\, \mathrm{tr}[\hat{\rho}^{\mathrm{I}}(T) \cdot e^{i\hat{H}^{\mathrm{F}}t} \hat{C} e^{-i\hat{H}^{\mathrm{F}}t}]. \tag{34}$$

A Fourier transform back into the time domain at the end of the calculation, finally, provides the desired time-dependent expectation value $C(t) = \int C(\omega) e^{-i\omega t}\, d\omega$ for $t \geqslant 0$. In order to obtain smooth data closer to the thermodynamic limit, a weak log-Gaussian broadening in frequency space quickly eliminates artificial oscillations in the time domain, which derive from the logarithmic discretization. Note that for the sole purpose of damping these artificial oscillations, typically a *significantly* smaller log-Gaussian broadening parameter $\alpha \lesssim 0.1$ suffices as compared to what is typically used to obtain fully smoothened correlation functions in the frequency domain (e.g., $\alpha \gtrsim 0.5$ for $\Lambda = 2$, see EPAPS of Ref. 14).

1. Lehmann representation

For the Lehmann representation of Eq. (34), in principle, three complete basis sets are required: one completed basis set i derived from an NRG run in $\hat{H}^{\mathrm{I}}$ to construct $\rho^{\mathrm{I}}(T)$, and two complete basis sets f and f' from an NRG run in $\hat{H}^{\mathrm{F}}$ to be inserted right before and after the $\hat{C}$ operator, respectively, to describe the dynamical behavior. Clearly, two NRG runs in $\hat{H}^{\mathrm{I}}$ and $\hat{H}^{\mathrm{F}}$ are required to describe the quantum quench.[6,7,39] With this, the spectral data in Eq. (34) becomes

$$C(\omega) = \sum_{i,f,f'} \underbrace{\langle f'|i\rangle}_{\equiv S^*_{if'}} \rho_c^{\mathrm{I}}(T) \underbrace{\langle i|f\rangle}_{\equiv S_{if}} C_{ff'}\, \delta\big(\omega - E^{\mathrm{F}}_{ff'}\big), \tag{35}$$

which generates the overlap matrix S. Now using the complete NRG eigenbasis sets together with the FDM, again similar to the fdmNRG in Eq. (29), this introduces another sum over Wilson shells. Therefore the fourier-transformed

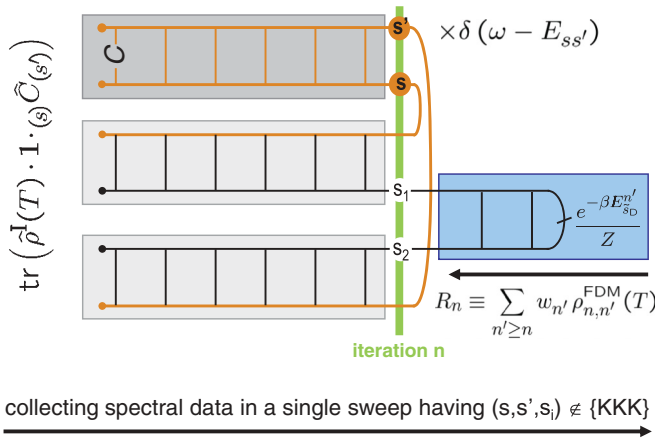

FIG. 7. (Color online) MPS diagram for the calculation of quantum quenches using tdmNRG [cf. Eq. (36)]. The calculation is performed in frequency space as depicted, which at the very end of the calculation is Fourier transformed back into the time domain to obtain the desired time-dependent expectation value $\hat{C}(t)$ [cf. Eq. (34)]. The calculation requires a complete eigenbasis for initial (black horizontal lines) and final Hamiltonian [orange (gray) horizontal lines], respectively, which are computed in two preceding NRG runs. Their respective shell-dependent overlap matrices S_n (two light gray boxes at lower left) are calculated in parallel to the calculation of the matrix elements C (dark gray box at the top). The projections R_n^{I} of the FDM (box at the lower right) are evaluated with respect to the initial Hamiltonian, but have exactly the same structure otherwise as already discussed with Fig. 6 [see also Eq. (21)]. The spectral data, finally, is collected in a full forward sweep, as indicated by the arrow at the bottom. To be specific, the summation is over all Wilson shells n and for a given iteration n, over all states $(s,s',s_i) \notin \{\mathrm{KKK}\}$ with $s_i \in \{s_1,s_2\}$.

time-dependent NRG (tdmNRG) becomes

$$C(\omega) = \sum_{n,ss'}{}' \left[S_n^\dagger R_n^{\mathrm{I},\tilde{\mathrm{X}}} S_n\right]_{s's} (C_n)_{ss'}\, \delta\left(\omega - E^n_{ss'}\right), \qquad (36)$$

where $(s,s') \in \{\mathrm{X},\mathrm{X}'\}$. In addition, $\tilde{\mathrm{X}} \in \{\mathrm{K},\mathrm{D}\}$ describes the sector of the reduced density matrix R_n^{I} from the initial system. To be specific, the notation for the first term in Eq. (36) implies the matrix product,

$$\left[S_n^\dagger R_n^{\mathrm{I},\tilde{\mathrm{X}}} S_n\right]^{\mathrm{X}'\mathrm{X}} \equiv \left(S_n^{\tilde{\mathrm{X}}\mathrm{X}'}\right)^\dagger \cdot R_n^{\mathrm{I},\tilde{\mathrm{X}}} \cdot S_n^{\tilde{\mathrm{X}}\mathrm{X}}. \qquad (37)$$

For example, the left daggered overlap matrix S_n selects the overlap of the sectors $\{\tilde{\mathrm{X}},\mathrm{X}'\}$ between initial and final eigenbasis, respectively. The prime in Eq. (36) indicates that the sum includes all combinations of sectors $\mathrm{XX}'\tilde{\mathrm{X}} \neq \mathrm{KKK}$, i.e., a total of seven contributions. The latter derives from the reduction of the independent threefold sum over Wilson shells [cf. Eq. (35)] into a single sum over Wilson shells n as discussed with Eq. (11). It is emphasized here, that the reduction of multiple sums in Wilson shells as in Eqs. (9) and (11) is *not* constrained to having the complete basis sets being identical to each other. It is easy to see that it equally applies to the current context of different basis sets from initial and final Hamiltonian.

The MPS diagram corresponding to Eq. (36) is shown in Fig. 7. It is similar to Fig. 6, yet with several essential differences: the block describing the matrix elements of the original operator $\hat{B}$ has now become the block containing $\hat{C}$. The original operator $\hat{C}^\dagger$ is absent, i.e., has become the identity. Yet since its "matrix elements" are calculated with respect to two different basis sets (initial and final Hamiltonian), an overlap matrix remains (lowest block in Fig. 7). In the context of the correlation functions in Fig. 6, the bra-ket states for the inserted complete basis set in the index s could be reduced to the single bra-index s, such that it affected a single horizontal line only. Here, however, two different complete basis sets hit upon each other, which inserts another overlap matrix (second block from the top in Fig. 7, which corresponds to the Hermitian conjugate of the lowest block). The reduced density matrices $R_n^{\mathrm{I,X}}$, finally, are built from the initial Hamiltonian, yet are completely identical in structure otherwise to the ones already introduced in Eq. (21).

The basis of the initial Hamiltonian enters through the two legs (horizontal black lines) in Fig. 7, which connect to the density matrix R_n. All other legs refer to the NRG basis generated by the final Hamiltonian [horizontal orange (gray) lines]. Finally, note that the plain contraction $S^\dagger R S$ of the lower three tensors with respect to the indices s_1 and s_2 can simply be evaluated through efficient matrix multiplication as in Eq. (37), while nevertheless respecting the selection rules on the state space sectors $\{\mathrm{X},\mathrm{X}',\tilde{\mathrm{X}}\} \neq \{\mathrm{K},\mathrm{K},\mathrm{K}\}$.

D. Fermi-golden-rule calculations

The NRG is designed for quantum impurity models. As such, it is also perfectly suited to deal with local quantum events such as absorption or emission of a generalized local impurity in contact with noninteracting reservoirs.[6,7,16,20,21,39] If the rate of absorption is weak, such that the system has sufficient time to equilibrate on average, then the resulting absorption spectra are described by Fermi's golden rule (fgr),[40]

$$A(\omega) = 2\pi \sum_{i,f} \rho_i^{\mathrm{I}}(T) \cdot |\langle f|\hat{C}^\dagger|i\rangle|^2 \cdot \delta(\omega - E_{if}), \qquad (38)$$

where i and f describe complete basis sets for initial and final system, respectively. The system starts in the thermal equilibrium of the initial system. The operator $\hat{C}^\dagger$ describes the absorption event at the impurity system, i.e., corresponds to the term in the Hamiltonian that couples to the light field. The transition amplitudes between initial and final Hamiltonian are fully described by the matrix elements $C_{if} \equiv \langle i|\hat{C}|f\rangle$. Given that the energy difference $E_{if} \equiv E_f^{\mathrm{F}} - E_i^{\mathrm{I}}$ in Eq. (38) needs to be calculated between states of initial and final system, absorption or emission spectra usually show threshold behavior in the frequency ω. The threshold frequency is given by the difference in the ground state energies of initial and final Hamiltonian, $\omega_{\mathrm{thr}} \equiv \Delta E_g \equiv E_g^{\mathrm{F}} - E_g^{\mathrm{I}}$, which eventually is blurred by temperature.

The difference between absorption and emission spectra is the reversed role of initial and final system, while also having $\hat{C}^\dagger \to \hat{C}$. That is, from the perspective of the absorption process, the emission process starts in the thermal equilibrium of the final Hamiltonian, with subsequent transition matrix elements to the initial system. This also implies that emission spectra have their contributions at negative frequencies, i.e., frequencies smaller than the threshold frequency ω_{thr} indicating the emission of a photon. Other than that, the

calculation of an emission spectrum is completely analogous to the calculation of an absorption spectrum. With this in mind, the following discussion will be therefore constrained to absorption spectra only.

While an absorption spectrum is already defined in frequency domain, it nevertheless can be translated into the time domain through Fourier transform,

$$\begin{aligned} A(t) &\equiv \int \frac{d\omega}{2\pi} e^{-i\omega t} A(\omega) \\ &= \sum_{i,f} \rho_i^{\mathrm{I}}(T) \cdot e^{iE_i t} \langle i|\hat{C}|f\rangle e^{-iE_f t} \cdot \langle f|\hat{C}^\dagger|i\rangle \\ &= \underbrace{\langle e^{i\hat{H}^{\mathrm{I}} t} \hat{C} e^{-i\hat{H}^{\mathrm{F}} t}}_{\equiv \hat{C}(t)} \cdot \hat{C}^\dagger \rangle_T^{\mathrm{I}}. \end{aligned} \tag{39}$$

Thus absorption spectra can also be interpreted similar to correlation functions and quantum quenches: at time $t = 0$, an absorption event occurs (application of the operator $\hat{C}^\dagger$, which for example rises an electron from a low lying level into some higher level that participates in the dynamics). This alters the Hamiltonian, such that the subsequent time evolution is governed by the final Hamiltonian. At some time $t > 0$ then, the absorption event relaxes back to the original configuration (application of $\hat{C}$). Therefore $A(t)$ essentially describes the overlap amplitude of the resulting state with the original state with no absorption within the thermal equilibrium of the initial system. While the "mixed" time evolution of $\hat{C}(t)$ in Eq. (39) may appear somewhat artificial at first glance, it can be easily rewritten in terms of a single time-independent Hamiltonian: by explicitly including a further static degree (e.g., a low lying hole from which the electron was lifted through the absorption event, or the photon itself), this switches $\hat{H}^{\mathrm{I}}$ to $\hat{H}^{\mathrm{F}}$, i.e., between two dynamically disconnected sectors in Hilbert space of the same Hamiltonian (compare discussion of type-1 and type-2 quenches in Ref. 22).

Within the FDM formalism, the Fermi-golden-rule calculations as defined in Eq. (38) becomes (fgrNRG),[20,21]

$$A(\omega) = \sum_{n,ss'}{}' \left[C_n^\dagger R_n^{\mathrm{I}}\right]_{s's} (C_n)_{ss'} \, \delta\left(\omega - E_{ss'}^n\right), \tag{40}$$

where $(s,s') \in \{\mathrm{X}^{\mathrm{I}}, \mathrm{X}^{\mathrm{F}}\} \notin \{\mathrm{KK}\}$. Therefore $(C_n)_{ss'} \equiv {}_n^{\mathrm{I}}\langle s|\hat{C}|s'\rangle_n^{\mathrm{F}}$ represents mixed matrix elements between states from initial and final Hamiltonian, respectively, which nevertheless can also be easily calculated using the basic contractions discussed with Fig. 4.

The MPS diagram to be evaluated for Eq. (40) is shown in Fig. 8. Its structure is completely analogous to the calculation of generic correlation functions in Fig. 6, except that similar to the quantum quench earlier, here again the basis sets from two different Hamiltonians come into play.[6,7,39] In contrast to the quantum quench situation in Fig. 7, however, no explicit overlap matrices are required. Instead, all matrix elements of the local operator $\hat{C}^\dagger$ themselves are mixed matrix elements between initial and final system. The reduced density matrices R_n^{I} are constructed with respect to the initial Hamiltonian, but again exactly correspond to the ones already introduced in Eq. (21) otherwise.

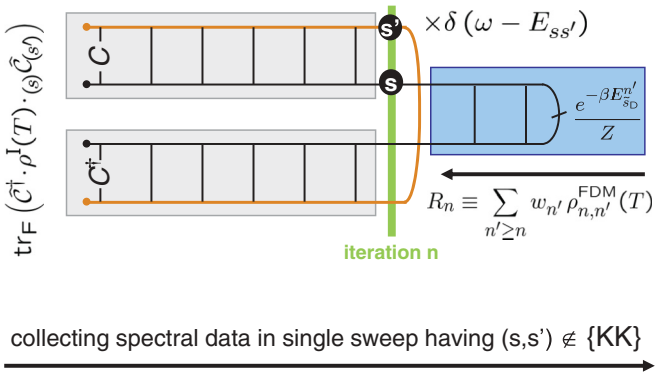

FIG. 8. (Color online) MPS diagram for the calculation of absorption spectra using Fermi's golden rule (fgrNRG) mediated by the operator $\hat{C}^\dagger$ [cf. Eq. (40)]. The two center legs (horizontal black lines) refer to the state space of the initial Hamiltonian, while the outer legs [horizontal orange (gray) lines] refer to the state space of the final Hamiltonian. Therefore the matrix elements of $\hat{C}^\dagger$ are *mixed* matrix elements between eigenstates of initial and final Hamiltonian.

1. Technical remarks

Absorption or emission spectra in the presence of Anderson orthogonality or strongly correlated low-energy physics typically exhibit sharply peaked features close to the threshold frequency with clear physical interpretation. While, in principle, a single Hamiltonian with dynamically disconnected Hilbert space sectors may have been used, this is ill-suited for an NRG simulation. Using a single NRG run, this can only resolve the low energy of the full Hamiltonian, i.e., of the initial system as it is assumed to lie lower in energy. Consequently, the sharp features at the threshold frequency will have to be smoothened by an energy window comparable to $\omega_{\mathrm{thr}} = \Delta E_g$ in order to suppress discretization artifacts. This problem is fully circumvented only by using two separate NRG runs, one for the initial and one for the final Hamiltonian.[6,7,39] With the NRG spectra typically collected in logarithmically spaced bins, having two NRG runs then, it is important that the data is collected in terms of the frequencies $\nu \equiv \omega - \omega_{\mathrm{thr}}$ taken *relative to the threshold frequency* ω_{thr} as defined earlier.

E. Higher-order correlation functions

Consider the spectral function of a three-point correlation function, which in the time domain is given by

$$\begin{aligned} A_{BCD}(t_1,t_2) &\equiv \langle \hat{D}(t_2)\hat{C}(t_1)\hat{B}\rangle_T \\ &\equiv \mathrm{tr}[\hat{\rho}(T) \cdot e^{i\hat{H}t_2} \hat{D} e^{i\hat{H}(t_1-t_2)} \hat{C} e^{-i\hat{H}t_1} \hat{B}]. \end{aligned} \tag{41}$$

Given a time-invariant Hamiltonian, the correlator of three operators $\hat{B}$, $\hat{C}$, and $\hat{D}$ acting at three different times results in the dependence on effectively two times t_1 and t_2, since t_0 as in $\hat{B}(t_0)$ can simply be chosen arbitrary, i.e., $t_0 = 0$ for simplicity.

Using the NRG eigenbasis sets together with the FDM, the Lehman representation of Eq. (41) requires four independent sums over complete eigenbasis sets, one from the FDM (X_ρ), and three by inserting an identity with every exponentiated Hamiltonian (X_1,X_2,X_3 from left to right), respectively. Again, with the reduced density matrix ρ being a scalar operator, one has $\mathrm{X}_\rho = \mathrm{X}_1$. Using Eq. (11) then, in frequency

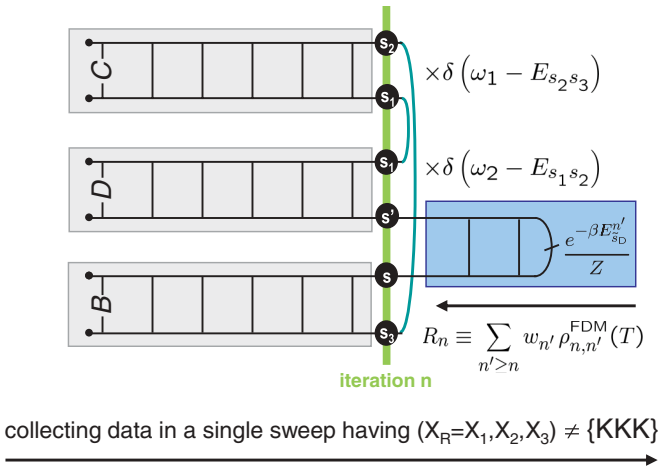

FIG. 9. (Color online) MPS diagram for the evaluation of a three-point correlation functions as in Eq. (42), which thus generalizes fdmNRG (see also Fig. 6).

space Eq. (41) becomes

$$A_{BCD}(\omega_1,\omega_2) = \sum_n {\sum_{s_1 s_2 s_3}}' [B_n R_n]_{s_3,s_1}(D_n)_{s_1 s_2}(C_n)_{s_2 s_3} \times \delta\left(\omega_2 - E^n_{s_1,s_2}\right)\delta\left(\omega_1 - E^n_{s_2,s_3}\right), \quad (42)$$

with $(s_1,s_2,s_3) \in \{X_1,X_2,X_3\} \neq \{KKK\}$, as indicated by the prime next to the sum, having $\left[B_n R_n\right]^{X_3,X_1} \equiv B_n^{X_3,X_1} R_n^{X_1}$. The MPS diagram corresponding to the spectral representation in Eq. (42) is shown in Fig. 9.

The more challenging part with Eq. (42) is the dependence on two frequencies. While the corresponding full collection of data into bins (ω_1,ω_2) can become expensive, however, certain fixed frequency points together with different kernels corresponding to a different analytic structure of the higher-order correlation function [which then replace the δ-functions in Eq. (42)], appear feasible with reasonable effort. Moreover, within the NRG context, by construction, one has comparable energy resolution for ω_1 and ω_2 at a given energy shell. Hence it remains to be seen in what respect vastly different energy scales of ω_1 as compared to ω_2, if required, are affected by the ansatz of energy scale separation within the NRG.

IV. SUMMARY AND CONCLUSIONS

The framework of tensor network has been applied to the NRG. This makes full use of the complete basis sets as introduced by Anders and Schiller,[10] which within the approximation of energy scale separation, also represent many-body eigenstates of the full Hamiltonian. Together with the full density matrix (FDM) approach, complete basis sets allow for simple transparent algorithms, as demonstrated for correlation function (fdmNRG), time-dependent quenches (tdmNRG) as well as Fermi-golden-rule (fgrNRG) calculations. The underlying principle is based on the plain Lehmann representation of the relevant dynamical expressions, which within the NRG, can be evaluated in a text-book-like clean and transparent fashion.

The framework of complete basis sets clearly allows for straightforward further generalizations. For example, one can envisage multiple consecutive time-steps that thus generalizes tdmNRG with the possibility to implement periodic switching.[41] While initially, the system starts in thermal equilibrium of a given Hamiltonian, after each quench the description of the system must be projected onto the complete basis set of the following Hamiltonian in terms of the reduced density matrix. For all these calculations, however, one must keep in mind that Wilson chains are not thermal reservoirs.[42] Within the tdmNRG, for example, this can manifest itself as *finite size effect*, in that already for a single quench in the absence of an external magnetic field, an initial excess spin at the impurity *cannot* be fully dissipated into the bath even in the limit of time $t \to \infty$, leading to (small) residual magnetization at the impurity. In cases where these discretization effects become a strong limiting factor, hybrid NRG approaches have been devised with the idea to extend the bath to a more refined or uniform spectrum. However, since this typically compromises energy scale separation along the full Wilson chain, other methods such as the DMRG need to be incorporated.[23,43]

ACKNOWLEDGMENTS

I want to thank Theo Costi, Markus Hanl, and Jan von Delft for their critical reading of the manuscript, and acknowledge fruitful discussions with Johannes Bauer on higher-order correlation functions. This work has received support from the German science foundation (TR-12, SFB631, NIM, and WE4819/1-1).

APPENDIX: FERMIONIC SIGNS

The NRG is typically applied to fermionic systems (for extensions to bosonic systems see, for example, Refs. 3, 44, and 45). Through its iterative prescription, the resulting MPS has a specific natural fermionic order in Fock space,

$$|s\rangle_n = \sum_{\sigma_d,\sigma_0,\ldots,\sigma_n} (A^{[\sigma_d]}A^{[\sigma_0]}\cdot\ldots\cdot A^{[\sigma_n]})_s \underbrace{|\sigma_n\rangle\ldots|\sigma_0\rangle|\sigma_d\rangle}_{\equiv|\sigma_n,\ldots,\sigma_0,\sigma_d\rangle}, \quad (A1)$$

where $|\sigma_d\rangle$ stands for the local state space of the impurity. Site $n' > n$ is added after site n, hence the state space $|\sigma_{n'}\rangle$ naturally appears to the left $|\sigma_n\rangle$ with second quantization in mind. The environmental states $|e\rangle_n$ with respect to iteration n which refers to the sites $n' > n$ is irrelevant for the following discussion, and hence will be skipped.

Let $\hat{c}^\dagger$ be a fermionic operator that acts on the impurity. Here, $\hat{c}^\dagger$ is assumed an arbitrary operator that nevertheless creates or destroys an odd number of fermionic particles such that fermionic signs apply. A very frequent task then is to represent this operator in the effective many-body basis at iteration n, i.e., to calculate the matrix elements $(C^\dagger_n)_{ss'} \equiv {}_n\langle s|\hat{c}^\dagger|s'\rangle_n$ [cf. Fig. 4]. This involves the basic matrix element with respect to local state spaces,

$$\langle\sigma_n,\ldots,\sigma_0,\sigma_d|\hat{c}^\dagger|\sigma'_n,\ldots,\sigma'_0,\sigma'_d\rangle = \left\{\prod_{i=n,\ldots,0}\underbrace{\left[\delta_{\sigma_i,\sigma'_i}(-1)^{n_{\sigma'_i}}\right]}_{\equiv(\hat{z}_i)_{\sigma_i,\sigma'_i}}\right\}\cdot\langle\sigma_d|\hat{c}^\dagger|\sigma'_d\rangle, \quad (A2)$$

with $\hat{z} \equiv (-1)^{\hat{n}} = \exp(i\pi\hat{n})$, akin to the Pauli z-matrix. That is, by pulling the operator $\hat{c}^\dagger$, acting on the impurity, to the right past the second quantization operators that create the states σ_{n_i}, fermionic signs apply, resulting in a *Jordan-Wigner string*

$$\hat{Z} \equiv \bigotimes_{i=0,\ldots,n} \hat{z}_i, \tag{A3}$$

to be called z-*string* in short. Note that through the Jordan-Wigner transformation, which maps fermions onto spins and vice versa, exactly the same string operator as in Eq. (A3) emerges. For a one-dimensional system with nearest-neighbor hopping, the Jordan-Wigner transformation to spins allows to eliminate on the operator level of the Hamiltonian further complications with fermionic signs. This is fully equivalent, of course, to the explicit treatment of the Jordan-Wigner string in a numerical setting that keeps a fermionic basis. The operators $\hat{z}_i$ in Eq. (A2) take care of the book keeping of fermionic signs, by inserting -1 $(+1)$ for all states σ_i at site i with odd (even) number of particles n_{σ_i}. The operators $\hat{z}_i$ are diagonal and hence commute with each other. In the case of additional explicit spin-degrees of freedom, such as the localized spin in the Kondo model, its z-operator is proportional to the identity matrix and hence can be safely ignored.

In the following, three alternative viewpoints are discussed for dealing with fermionic signs in the MPS setup of the NRG. To be specific, the following discussion assumes $\hat{c}^\dagger = \hat{d}^\dagger$ which creates a particle at the impurity's d level. As such, it generates a Jordan Wigner string for all sites added subsequently to the MPS, i.e., sites $i = 0, \ldots, n$ [cf. Eq. (A3)].

1. Viewpoint 1: Rerouting of z-string in tensor network

Figure 10 depicts an MPS diagram for the typical evaluation of matrix elements with relevant fermionic signs. The A-tensors that derive from a preceeding iterative state space generation of the NRG are depicted by the ternary nodes (cf. Fig. 4). By keeping track of the total number n of particles for all indices then, for some specific index a the fermionic sign is given by $(-1)^{n_a}$.

The z-string that is required for the evaluation of the matrix elements of $d^\dagger$, stretches across all local state spaces σ_i with $0 \leqslant i \leqslant n$. This is depicted by the light green (gray) line in Fig. 10 (note that this is not the extra index that takes care of non-Abelian symmetries as in Fig. 5, even though graphically its role is not that dissimilar). Here, the interpretation is such, that a *crossing* of the z-string with a state space inserts fermionic signs for this state space.[46–48] Consider then, for example, the upper right A-tensor, A_n, in Fig. 10. For simplicity, its three legs are labeled $l \equiv s_{n-1}$ (state space from previous iteration), $\sigma_{(n)}$ (new local state space), and $r \equiv s_n$ (combined state space) for left, local, and right, respectively. By tracking the total particle number for all states, given the left-to-right orthonormalization (see arrows in Fig. 4), by construction it must hold $n_l + n_\sigma = n_r$. The index σ is *crossed* by the z-string, hence fermionic signs apply at the location of the crossing,

$$z_\sigma \equiv (-1)^{n_\sigma} = (-1)^{n_r} \underbrace{(-1)^{-n_l}}_{=(-1)^{+n_l}} \equiv z_l z_r. \tag{A4}$$

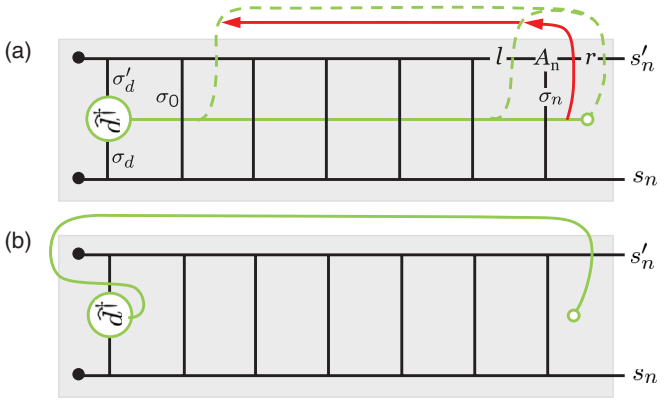

FIG. 10. (Color online) MPS diagrams and fermionic signs. Consider the matrix elements of a local operator $\hat{d}^\dagger$ which creates a particle at the impurity, i.e., the first local state space of the MPS in the effective MPS space $|s\rangle_n$. A z-string (Jordan-Wigner string) $\hat{Z} = \bigotimes_i \hat{z}_i$ arises [green (gray) horizontal line in the middle]. The endpoints (open circles) indicate the range of the z-string, i.e., starting from and including site 0 to site n. For every crossing of the z-string with a black line, which represent state spaces, fermionic signs apply. (a) shows that a z-string can be rerouted (light dashed lines, pushed in the direction of the red arrow). The resulting configuration in (b) shows that by rerouting the z-string significantly fewer crossings with black lines can be achieved. In particular, the z-strings, which applied to all sites to the right of $\hat{d}^\dagger$ (a), can be significantly reduced to local fermionic signs at the impurity and another fermionic sign with the state space s_n.

Therefore, instead of applying fermionic signs with index σ, it is equally correct to apply fermionic signs with the indices l and r. This allows to *reroute* the z-string[46–48] as indicated in Fig. 10 (dashed line to the upper right with the shift in the z-string indicated by short red arrow). Note that for this rerouting to work, the actual left-to-right orthonormalization is not strictly required, and could be relaxed, in general, to the more general condition $n_l \pm n_r \pm n_\sigma =$ even. In particular, this includes $n_l \pm n_r \pm n_\sigma = 0$, which suggests that *any* direction of orthonormalization is acceptable, together with a generic *current site* that combines all (effective) state spaces to an even number of particles, i.e., $n_l + n_r + n_\sigma = n_{\text{tot}} =$ even (for $n_{\text{tot}} =$ odd, a global minus sign would apply in the case of rerouting).

The basic rerouting step as indicated above can be repeated, such that the z-string can be pulled to the top outside the MPS diagram in Fig. 10(a), with the final configuration shown in Fig. 10(b). The state to the very left (black dot) is the vacuum states with no particles, hence the z-string can be fully pulled outside at the left. As a result, instead of the original n crossings with the state space σ_n, only two crossings of the z-string with state spaces (black lines) remain: one crossing with the local state space at the impurity itself, leading to

$$\hat{d}^\dagger \to \hat{d}^\dagger \hat{z}_d \equiv (\hat{z}\hat{d})^\dagger, \tag{A5}$$

which fully acts within the state space of the impurity, and another crossing with the state space $|s'\rangle_n$ at iteration n.

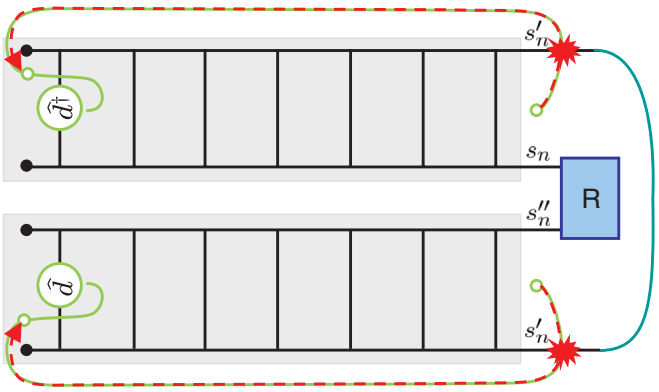

FIG. 11. (Color online) Fermionic signs in correlation functions. Two MPS diagrams as in Fig. 11 for the matrix elements of $\hat{d}$ and $\hat{d}^\dagger$ are combined, as required, for example, for the calculation of correlation functions. The resulting product of matrix elements ${}_n\langle s'|\hat{d}|s''\rangle_n \cdot R^{[n]}_{s'',s} \cdot {}_n\langle s|\hat{d}^\dagger|s'\rangle_n$ leads to cancellation of the fermionic signs in the index s' in the rerouted z-strings (light green lines), as indicated by the two splashes to the right. Hence the right end-point of the z-string can be fully retracted to the very left of the diagram, as indicated by the dashed red arrows. The partial contribution R to the FDM is a scalar operator, such that assuming charge conservation, the particle number of the states s and s'' also must be same. Hence the z-string in Fig. 11 could have been equally well also rerouted downwards, instead. The respective fermionic signs with states s and s'' still would have canceled, while the order of application of the z-operator with the impurity would have changed.

In typical applications which include thermal expectation values or correlation functions, however, an operator $\hat{d}^\dagger$ never comes by itself, as its expectation value with respect to any state with well-defined particle number would be zero. Therefore creation and annihilation operators always appear in pairs. For the local spectral function, for example, $\hat{d}^\dagger$ is paired with its daggered version $\hat{d}$. In their overall combination, the fermionic signs with respect to the index s' appear *twice* and hence annihilate each other. This situation is sketched in Fig. 11. The matrix element discussed previously with Fig. 10 is shown in the upper half of the figure. Given the case of spectral functions (cf. Fig. 6), its counterpart is shown at the bottom. The reduced density matrix R is a scalar operator, such that the particle number of the states s and s'' must match. Similarly, the outer two states are connected through the overall trace (solid line to the very right), hence refer to exactly the same state. Consequently, the same fermionic sign factor applies twice with the rerouted z-strings, which thus cancels, i.e., $[(-1)^{n_s}]^2 = 1$ (indicated by the two splashes with s' at the right). Consequently, the right end-point of the z-strings can be retracted along the rerouted z-string all to the way to the left of the impurity (indicated by the red dashed arrow).

Therefore given the A-tensors for the basis transformations from a prior NRG run that only generates the basis, above line of argument allows to ignore fermionic signs for most of the subsequent calculation of thermodynamic quantities or spectral properties. Specifically, in given example which applies to fdmNRG, tdmNRG, as well as fgrNRG, it is sufficient to calculate the spectral functions for the operator $\hat{d} \to \hat{z}_d\hat{d}$ [cf. Eq. (A5)] and *fully ignore* fermionic signs for the rest of the chain. This is in contrast to the original setup where the full z-string needs to be included.

2. Viewpoint 2: Operator representation

An alternative way to demonstrate the effect of rerouting of the z-string can be given by looking at the equivalent (numerical) tensor-product representation of operators in the full many-body Hilbert space without making reference to MPS notation. Given the fermionic order of sites as in Eq. (A1), a fermionic operator $\hat{c}_k$ that destroys a particle at site k, has the tensor-product form

$$\hat{C}_k \equiv \hat{1}_d \otimes \hat{1}_0 \otimes \ldots \hat{1}_{k-1} \otimes \hat{c}_k \otimes \hat{z}_{k+1} \otimes \ldots \otimes \hat{z}_n, \qquad \text{(A6)}$$

where $\hat{1}_i$ is the identity matrix at site i, $\hat{c}_k$ the desired operator acting within the state space of site k, and $\hat{z}_i \equiv (-1)^{\hat{n}_i}$ as in Eq. (A2). Now, applying a z-operator to the states s' at the last site n is equivalent to applying a z-operator to each individual site,

$$\begin{aligned}\hat{Z}\hat{C}_k &\equiv \Big(\bigotimes_{i=d}^{n} \hat{z}_i\Big)\hat{c}_k \\ &= \hat{z}_d \otimes \hat{z}_0 \otimes \ldots \hat{z}_{k-1} \otimes [\hat{z}\hat{c}]_k \otimes \hat{1}_{k+1} \ldots \hat{1}_n, \qquad \text{(A7)}\end{aligned}$$

since $(\hat{z}_i)^2 = \hat{1}_i$. In the application to thermodynamic quantities such as correlations functions, the operator $\hat{C}_k$ would again appear together with its daggered version $\hat{C}_k^\dagger$, hence insertion of $\hat{Z}^2$ has no effect, yet can be split in equal parts, i.e., $\hat{C}_k^\dagger\hat{C}_k = (\hat{Z}\hat{C}_k)^\dagger(\hat{Z}\hat{C}_k)$. Therefore, $\hat{Z}\hat{C}_k$ can be equally well used instead of $\hat{C}_k$. As a result, similar to Fig. 11, the z-strings have again been fully flipped from the sites to the right of site k to the left of site k, with the additional transformation $\hat{c}_k \to [\hat{z}\hat{c}]_k$. Note that, essentially, this equivalent to fully reverting the fermionic order.

3. Viewpoint 3: Auxiliary fermionic level

In the case of absorption spectra, the absorption of a photon creates an electron-hole pair, $\hat{h}^\dagger\hat{d}^\dagger$, where the hole $\hat{h}^\dagger$ can be simply treated as a spectator in the dynamics. Nevertheless, by explicitly including the hole in the correlation function, i.e., by using the operator $\hat{d}^\dagger \to \hat{h}^\dagger\hat{d}^\dagger$, this operator itself now already forms a pair of fermions that preserves particle number (assuming that $\hat{h}^\dagger$ creates a hole). Therefore, by construction, $\hat{h}^\dagger\hat{d}^\dagger$ simply commutes with all Wilson sites except for the impurity upon which it acts.

The same argument can be repeated for a standard spectral function, by introducing an auxiliary fermionic level $\hat{h}$ that does not participate in the dynamics, i.e., does not appear in the Hamiltonian. In general, *prepending* the states in Eq. (A1) by the states $|\sigma_h\rangle$ of the "hole", i.e.,

$$|\sigma_n, \ldots, \sigma_0, \sigma_d\rangle \to |\sigma_n, \ldots, \sigma_0, \sigma_d\rangle|\sigma_h\rangle, \qquad \text{(A8)}$$

immediately results in the same consistent picture as already encountered with Fig. 11 or Eq. (A7).

[1]K. G. Wilson, Rev. Mod. Phys. **47**, 773 (1975).
[2]H. R. Krishna-murthy, J. W. Wilkins, and K. G. Wilson, Phys. Rev. B **21**, 1003 (1980).
[3]R. Bulla, T. Costi, and T. Pruschke, Rev. Mod. Phys. **80**, 395 (2008).
[4]T. A. Costi and A. C. Hewson, Philos. Mag. B **65**, 1165 (1992).
[5]T. A. Costi, Phys. Rev. B **55**, 3003 (1997).
[6]L. N. Oliveira and J. W. Wilkins, Phys. Rev. B **24**, 4863 (1981).
[7]L. N. Oliveira and J. W. Wilkins, Phys. Rev. B **32**, 696 (1985).
[8]O. Sakai, Y. Shimizu, and T. Kasuya, J. Phys. Soc. Jpn. **58**, 3666 (1989).
[9]W. Hofstetter, Phys. Rev. Lett. **85**, 1508 (2000).
[10]F. B. Anders and A. Schiller, Phys. Rev. Lett. **95**, 196801 (2005).
[11]S. R. White and A. E. Feiguin, Phys. Rev. Lett. **93**, 076401 (2004).
[12]A. J. Daley, C. Kollath, U. Schollwöck, and G. Vidal, J. Stat. Mech.: Theory Exp. (2004) P04005.
[13]R. Peters, T. Pruschke, and F. B. Anders, Phys. Rev. B **74**, 245114 (2006).
[14]A. Weichselbaum and J. von Delft, Phys. Rev. Lett. **99**, 076402 (2007).
[15]A. Weichselbaum, Phys. Rev. B **84**, 125130 (2011).
[16]A. Weichselbaum, W. Münder, and J. von Delft, Phys. Rev. B **84**, 075137 (2011).
[17]A. I. Tóth, C. P. Moca, Ö. Legeza, and G. Zaránd, Phys. Rev. B **78**, 245109 (2008).
[18]C. P. Moca, A. Alex, J. von Delft, and G. Zaránd, Phys. Rev. B **86**, 195128 (2012).
[19]T. A. Costi, L. Bergqvist, A. Weichselbaum, J. von Delft, T. Micklitz, A. Rosch, P. Mavropoulos, P. H. Dederichs, F. Mallet, L. Saminadayar *et al.*, Phys. Rev. Lett. **102**, 056802 (2009).
[20]H. E. Türeci, M. Hanl, M. Claassen, A. Weichselbaum, T. Hecht, B. Braunecker, A. Govorov, L. Glazman, A. Imamoglu, and J. von Delft, Phys. Rev. Lett. **106**, 107402 (2011).
[21]C. Latta, F. Haupt, M. Hanl, A. Weichselbaum, M. Claassen, W. Wuester, P. Fallahi, S. Faelt, L. Glazman, J. von Delft *et al.*, Nature (London) **474**, 627 (2011).
[22]W. Münder, A. Weichselbaum, M. Goldstein, Y. Gefen, and J. von Delft, Phys. Rev. B **85**, 235104 (2012).
[23]A. Weichselbaum, F. Verstraete, U. Schollwöck, J. I. Cirac, and J. von Delft, Phys. Rev. B **80**, 165117 (2009); F. Verstraete, A. Weichselbaum, U. Schollwöck, J. I. Cirac, and J. von Delft, arXiv:cond-mat/0504305v1.
[24]U. Schollwöck, Ann. Phys. **326**, 96 (2011).
[25]L. N. Oliveira, Braz. J. Phys. **22**, 155 (1992).
[26]R. Žitko and T. Pruschke, Phys. Rev. B **79**, 085106 (2009).
[27]J. Friedel, Adv. Phys. **3**, 446 (1954).
[28]J. Friedel, Nuovo Cimento Suppl. **7**, 287 (1958).
[29]P. W. Anderson, Phys. Rev. **124**, 41 (1961).
[30]P. W. Anderson, Phys. Rev. Lett. **18**, 1049 (1967).
[31]H. Saberi, A. Weichselbaum, and J. von Delft, Phys. Rev. B **78**, 035124 (2008).
[32]S. R. White, Phys. Rev. Lett. **69**, 2863 (1992).
[33]U. Schollwöck, Rev. Mod. Phys. **77**, 259 (2005).
[34]F. Verstraete, V. Murg, and J. Cirac, Adv. Phys. **57**, 143 (2008).
[35]M. M. Wolf, F. Verstraete, M. B. Hastings, and J. I. Cirac, Phys. Rev. Lett. **100**, 070502 (2008).
[36]N. Schuch, M. M. Wolf, F. Verstraete, and J. I. Cirac, Phys. Rev. Lett. **100**, 030504 (2008).
[37]A. Weichselbaum, Ann. Phys. **327**, 2972 (2012).
[38]A. Alex, M. Kalus, A. Huckleberry, and J. von Delft, J. Math. Phys. **52**, 023507 (2011).
[39]R. W. Helmes, M. Sindel, L. Borda, and J. von Delft, Phys. Rev. B **72**, 125301 (2005).
[40]J. J. Sakurai, *Modern Quantum Mechanics* (Addison-Wesley Publishing Company, Reading, MA, 1994).
[41]E. Eidelstein, A. Schiller, F. Güttge, and F. B. Anders, Phys. Rev. B **85**, 075118 (2012).
[42]A. Rosch, Eur. Phys. J. B **85**, 6 (2011).
[43]F. Guettge, F. B. Anders, U. Schollwoeck, E. Eidelstein, and A. Schiller, arXiv:1206.2186v1.
[44]R. Bulla, N.-H. Tong, and M. Vojta, Phys. Rev. Lett. **91**, 170601 (2003).
[45]C. Guo, A. Weichselbaum, J. von Delft, and M. Vojta, Phys. Rev. Lett. **108**, 160401 (2012).
[46]P. Corboz, R. Orús, B. Bauer, and G. Vidal, Phys. Rev. B **81**, 165104 (2010).
[47]C. V. Kraus, N. Schuch, F. Verstraete, and J. I. Cirac, Phys. Rev. A **81**, 052338 (2010).
[48]T. Barthel, C. Pineda, and J. Eisert, Phys. Rev. A **80**, 042333 (2009).